Tsunami detection method using high-frequency ocean surface radar

Ryotaro Fuji

2017

Tsunami detection method using high-frequency ocean surface radar

A Dissertation

Submitted for the Degree of

Doctor of Engineering

by

Ryotaro Fuji

Ehime University

September 2017

Abstract

Mitigating disasters caused by huge tsunamis is a particularly crucial issue in Japan. High-frequency ocean surface radar (HF radar) provides the great advantage of observing a wide range of ocean surface currents. It could be useful for tsunami mitigation and yet few studies have been conducted. This research examines the tsunami detection performance of HF radar by using a novel technique—a virtual tsunami observation experiment—with the aim of establishing a real-time tsunami detection method.

Regarding tsunami detection, the combination of HF radar and a tsunami detection method should be assessed as the onshore-offshore distribution of tsunami detection probability, because the probability will vary in accordance with the signal-to-noise ratio (SNR) and the tsunami magnitude in addition to the radar system specifications. We statistically examined the tsunami detection distance and earliness of detection based on virtual tsunami observation experiments by using signals received in February 2014 by HF radar installed on the southern coast of Japan and numerically simulated velocities induced by a Nankai Trough earthquake. In the experiments, the Doppler frequencies associated with the simulated velocities were superimposed on the receiving

signals of the radar, and the radial velocities were calculated from the synthesized signals by the fast Fourier transform. A tsunami was then detected based on the temporal change in the cross-correlation of the velocities, before and after tsunami arrival, between two points 3 km apart along a radar beam.

First, the tsunami detection performance of the present method combined with the HF radar was examined through *a posteriori* analysis according to the above procedure. We found that the possibility of tsunami detection primarily depends on the kinetic energy ratio between tsunami current and background current velocities. The monthly average detection probability is over 90% when the energy ratio exceeds 5 (offshore distance: $9\ \mathrm{km} \leq L \leq 36\ \mathrm{km}$) and is reduced to 50% when the energy ratio is approximately 1 ($L = 42$ km) over the continental shelf slope. The ratio varied with the background current physics and SNR, which was mainly affected by ocean surface wave heights and ionospheric electron density. The variance reduction representing the degree of coincidence between radar and simulated velocities was over 80% in the ranges where the tsunami was detected, and less than 10% in ranges where the tsunami was not detected. Thus, we can use the detected tsunami velocities to mitigate tsunami impact, such as to check the category of tsunami warning issued by the JMA, estimate tsunami height along the coast, and estimate the tsunami source based on the inversion

method and thus specify areas at risk of devastating damage by numerical simulation, in addition to tsunami detection.

Secondly, earliness of tsunami detection was examined through real-time analysis. We found that the possibility of tsunami wavefront detection primarily depends on the kinetic energy ratio even in real-time detection. However, the energy ratio required for tsunami wavefront detection is one order of magnitude less than that by *a posteriori* analysis. The maximum detection distance with 80% detection probability and 4-min time lag was 22.5 km (corresponding energy ratio is of the order of 10^0). Tsunami arrival was detected approximately within 3–5 min after the time of manifestation of tsunami-induced velocity in ranges from 3 to 22.5 km with 80% probability. The established method is outstanding in terms of detecting subsequent tsunami wavetrains in addition to tsunami wavefront, with no misdetection.

Contents

Chapter 1

Introduction

1.1 Tsunami detection by HF radar

Researchers in Japan, the USA, Chile and Germany have succeeded in detecting the variability of tsunami velocities induced by the March 11, 2011 Tohoku-Oki earthquake by using high-frequency ocean surface radars (HF radars; Dzvonkovskaya et al. 2011, 2012; Hinata et al. 2011, 2012; Lipa et al. 2011). Hinata et al. (2011, 2012) detected the flow velocity fluctuations due to the incoming tsunami at about 30 km off the coast and subsequent resonances by using HF radars installed on the eastern coast of the Kii Channel, at a distance of about 1000 km from the epicenter. The radar-observed amplitude of the fluctuations was about 10 cm/s. Lipa et al. (2011) detected the tsunami-induced current velocities on the southwestern coast of Hokkaido in Japan and on the western coast of California in the USA. The research groups in Chile and Germany detected the velocity of the tsunami upon its arrival at the western coast of Chile 22 h after the earthquake (Dzvonkovskaya et al. 2011). They demonstrated that the radial velocities observed by the HF radar were highly correlated with the tsunami

wave heights (heights from trough to crest) recorded by a tide gauge installed about 50 km off the coast, with maximum cross-correlation values of 0.5–0.7 on the continental shelf edge. These observations have provided a clear answer as to whether or not tsunami detection is possible by using HF radars, an issue that has been discussed for more than 30 years (e.g., Barrick 1979; Lipa et al. 2006).

Huge earthquakes along the Nankai Trough with a moment magnitude (M_w) of about 9.0 are expected on the southern coast of Japan with a probability of about 60–88% (88% for a Tokai earthquake, 70% for a Tonankai earthquake, 60% for a Nankai earthquake) in the next 30 years (Japan Cabinet Office). The earthquakes will induce strong tsunami currents and thus it is essential to determine the arrival of the first tsunami wave further offshore—tsunami detection—to mitigate the impact of the tsunami. The maximum detection distance of tsunamis induced by huge earthquakes cannot be determined based on past observation results, because the maximum distance will vary in accordance with the signal-to-noise ratio (SNR) of the receiving signals of the radars and/or the tsunami-induced current velocities upon arrival as well as the radar system specifications. Hence, the maximum tsunami detection distance and earliness of detection for the radar system at a certain location must be statistically analyzed with various SNR values and tsunami magnitudes.

Following the actual measurements of the 2011 Japan tsunami, tsunami detection techniques with HF radars have been developed (e.g., Lipa et al. 2012a, b, 2014; Fuji et al. 2015; Grilli et al. 2015, 2016). Lipa et al. (2012a) proposed a tsunami detection algorithm using the CODAR SeaSonde® system based on pattern recognition, which uses the temporal change of cross-correlation of the spatially averaged velocities within 2–6-km wide bands parallel to the coast. They applied the algorithm to the 2011 Japan tsunami and showed that the approaching tsunami could be detected in regions where the water depth is less than 200 m within the radar coverage area, and that advance warnings could have been issued approximately 8 min (i.e., twice the HF radar spectral time resolution) after its arrival. They also concluded that the method could have detected the 2012 Indonesian tsunami (Lipa et al. 2012b).

Fuji et al. (2015) detected a tsunami using the Nagano Japan Radio Co., Ltd. (NJRC) radar system (Table 2.1) based on the temporal change in the cross-correlation of radial velocities with zero time lag, before and after the arrival of the tsunami, between two observation points in the radial direction, assuming that a M_w 9.0 Nankai Trough earthquake (Japan Cabinet Office's fault model case 3) occurred at 00:00 on April 5, 2014. They showed that the maximum tsunami detection distance was 52.5 km

offshore when Δr (distance between the two points) = 3.0 km. However, a statistical analysis was not implemented.

These two methodologies for detecting tsunami are based on the spatial correlation of tsunami-induced velocities. In contrast, Grilli et al. (2015) proposed a method for tsunami detection based on the time correlation of the Bragg resonant backscattering signals of the HF radar (Stradivarius system) along a tsunami wave-ray considering various wind speeds and environmental noise levels. They verified the method by using simulated receiving signals, idealized tsunami wavetrains and a simple seafloor geometry, and demonstrated the possibility of tsunami detection beyond the continental shelf where the tsunami-induced velocities are rather small. Grilli et al. (2016) applied the algorithm to realistic case studies and validated it, in which bathymetry offshore of Vancouver Island was used and the tsunami was induced by a displacement of the sea floor in a seismic source region.

1.2 Key for tsunami detection in Japan

As mentioned above, the combination of a tsunami detection method and a radar system should be assessed by its tsunami detection probability distribution with respect to the distance from the coast. However, no previous studies have discussed the distance

and the earliness statistically based on a number of tsunami observations. This is because actual tsunami detection using HF radars is limited to the 2011 Japan and the 2012 Indonesian tsunamis except for some meteotsunami observations (e.g., Lipa et al. 2014). Considering the low probability of tsunami occurrence, it is unlikely to be possible to obtain many more tsunami observations in the near future.

Three minutes after the 2011 Tohoku-Oki earthquake, the first warning, which underestimated the tsunami height (sea surface displacement induced by the tsunami), was issued by the Japan Meteorological Agency (JMA). The JMA revised the category of warning upward 28 min after the earthquake (Ozaki 2011) based on the tsunami heights measured by a GPS wave gauge (NOWPHAS: Nationwide Ocean Wave Information Network for Ports and Harbours, http://www.mlit.go.jp/kowan/nowphas/index_eng.html) installed off the Tohoku coast. The underestimation, which eventually led to greater damage (e.g., Takahashi and Konuma 2011; Seto and Takahashi 2015), was caused by saturation of the magnitude calculated by seismometer measurements. No other tsunami warning system is in operation in Japan except that of the JMA. The underestimation of a tsunami warning is a major concern for the huge tsunamis with a maximum tsunami height exceeding 30 m estimated to be generated by Nankai Trough earthquakes. Therefore, in addition to

detecting the tsunami arrival offshore, it is crucial to estimate tsunami heights and check the category of tsunami warning issued by the JMA by using measured tsunami heights or tsunami-induced velocities in order to mitigate and understand the impacts of tsunamis in coastal regions. Moreover, it is also crucial to examine the earliness of tsunami detection since the tsunamis induced by Nankai Trough earthquakes are expected to reach the coast within a few minutes.

1.3 Purpose of this study

This study examines the tsunami detection performance of the combination of the present method and the NJRC radar system by using a novel technique—virtual tsunami observation experiment—with the aim of establishing a real-time tsunami detection method. We conditionally examined detection probability by using 1-month observation signals on the Mihama coast in February 2014 and assuming a scenario of the fault model case 3 of a Nankai Trough earthquake.

The flow of this study is shown in Fig. 1.1 and this paper is organized as follows: first, as described in Chapter 2, we performed virtual tsunami observation experiments through *a posteriori* analysis using signals received by the NJRC radar (Table 2.1) installed on the Mihama coast (Fig. 2.1) and a Nankai Trough tsunami simulation based

on the fault model case 3 in order to overcome the difficulty of obtaining more tsunami observations and to statistically examine the detection distance and quantitatively examine the nearshore tsunami heights inferred from offshore velocities. In these experiments, Doppler frequencies associated with the tsunami-induced current velocities simulated by a numerical model were superimposed on the receiving signals actually observed during February 2014 by using the method proposed by Gurgel et al. (2011). The synthesized signals were analyzed and radial velocities were calculated by the fast Fourier transform (FFT). The tsunami was then detected by using a method similar to that in Fuji et al. (2015). We then assessed the combination of the NJRC radar system and the detection method mainly by using detection probability with respect to the offshore distance from the radar. Also, we quantitatively examined the measured tsunami-induced velocities (i) by comparing the tsunami warning categories inferred from the numerical simulation and from the offshore velocity measurements by the radar, and (ii) by estimating the degree of coincidence of the observed and simulated velocity variability using variance reduction. Next, as described in Chapter 3, we performed virtual tsunami observation experiments through a real-time analysis, and assessed the earliness of detecting the tsunami wavefront. The detection results were compared with the previous method using q-factor proposed by Lipa et al. (2012a, b,

2014) and the applicability of the method was discussed. Finally, some conclusions are drawn in Chapter 4.

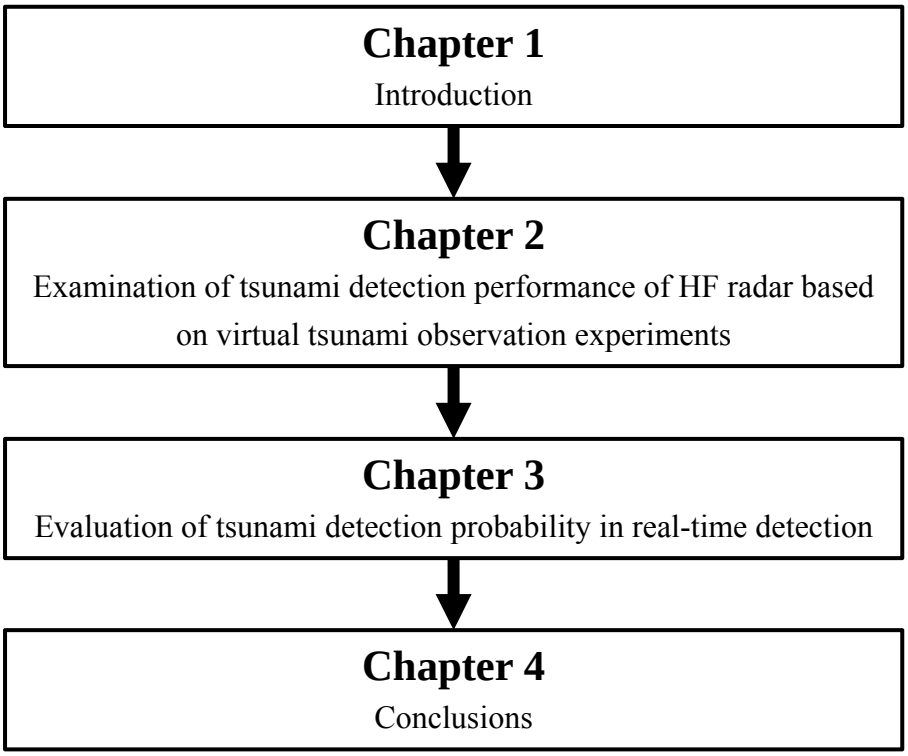

Fig. 1.1 Flow of this study

Chapter 2

Examination of tsunami detection performance of HF radar based on virtual tsunami observation experiments

2.1 Introduction

In this chapter, we propose a novel method for detecting tsunami by using cross-correlation of tsunami-induced velocities observed by HF radar. To overcome the difficulty of obtaining more tsunami observations in the near future, virtual tsunami observation experiments were employed. This method allows us to quantitatively measure offshore velocity variability induced by a huge tsunami in addition to detecting the tsunami.

2.2 Materials and methods

2.2.1 HF radar observation on and beyond the continental shelf of the Kii Channel

In the virtual tsunami observation experiments, we used background current (BGC; e.g., tidal current, wind-driven current, Kuroshio) signals actually observed by the NJRC radar that had been installed on the Mihama coast from September 2012 to

February 2016 (Fig. 2.1). No detectable tsunamis occurred during the period. This radar system is the same type as that used by Hinata et al. (2011, 2012) and identical to the radar in Fuji et al. (2015). The system specifications are shown in Table 2.1. The center frequency of the transmitting wave is 24.515 MHz, sweep bandwidth is 100 kHz, frequency sweep interval is 0.5 s, range resolution in the radial direction is 1.5 km, and bearing (azimuthal) resolution is 7.5°. Radial velocities within 64 range cells (extending 96 km offshore from the HF radar location) are calculated (Fig. 2.1c). The system performs the FFT and calculation of surface current velocities from the receiving signals in parallel with the continuous transmission of signals. This enables us to obtain the velocities every 1 min.

Receiving signals measured in February 2014 along beam 04 (solid line in Fig. 2.1a), which was directed approximately toward the south, were analyzed. Water depths along beam 04 are approximately 200 m at cell 19 (28 km offshore), 1000 m at cell 27 (40 km offshore), and 2000 m at cell 64 (96 km offshore). The continental shelf edge is located around 30 km offshore (cell 20). Significant wind wave heights observed by the Wakayama-Nanseioki GPS wave gauge of NOWPHAS located 28.5 km offshore (cell 19) were used to examine SNR variability dynamics. In February, the monthly average significant wave height was the highest of 2014. In addition, variability of

ionospheric intensity (i.e., electron density) observed by the National Institute of Information and Communications Technology (NICT) at ionosphere observation stations (Fig. 2.1b) was investigated.

2.2.2 Simulation of tsunami generated by a M_w 9.0 Nankai Trough earthquake

We simulated the time series of tsunami velocities in the seas around Japan (Fig. 2.3a) by using a numerical model, which was originally developed by Goto et al. (1997) and has been widely used for tsunami calculations (e.g., Takahashi et al. 1995; Imai et al. 2010; Sugawara and Goto 2012). The governing equations are the linear long-wave equation and continuity equation with a perfect reflection boundary condition along the coast line:

$$\frac{\partial \eta}{\partial t} + \frac{\partial M}{\partial x} + \frac{\partial N}{\partial y} = 0 \quad , \tag{1}$$

$$\frac{\partial M}{\partial t} + gh\frac{\partial \eta}{\partial x} = 0 \quad , \tag{2}$$

$$\frac{\partial N}{\partial t} + gh\frac{\partial \eta}{\partial y} = 0 \quad . \tag{3}$$

where η is the water level, h is the water depth, and M, N are the flow flux in the east–west and north–south directions, respectively. The spatial resolution is 1 km and the

calculation time step is 0.5 s, corresponding to the frequency sweep interval of the radar system (Table 2.1).

We selected the Japan Cabinet Office's fault model case 3 from cases 1 to 11 of the Nankai Trough earthquake. This fault model has a large slip area with a maximum slip of 45 m, which occurs in the shallow part of the fault near the trough axis off the Kii Channel (Fig. 2.3a). The M_w 9.0 case 3 earthquake generates the maximum tsunami heights among the 11 cases along the coast within the radar coverage. The initial sea surface level was set by calculating the ocean bottom deformation with Okada's formula (Okada 1992; Fig. 2.3a). The maximum initial sea surface level is approximately 10 m. No BGCs (e.g., tidal current, wind-driven current, Kuroshio) were included in the simulation.

In total, 660 tsunami event cases were considered: the timing of the tsunami event was set from 06:00 February 1, 2014 to 17:00 February 28, 2014 at 60-min intervals. In each case, the case 3 tsunami was used. In other words, each event has a different timing of tsunami occurrence. The first tsunami wave passed through the radar coverage within 30 min after the earthquake (Fig. 2.3a). The tsunami propagates approximately along beam 04, which is almost perpendicular to the depth contours, and refracts towards the coast on the continental shelf. The maximum tsunami heights significantly

increased near the coast due to wave shoaling, which was as high as around 7 m at cell 3 (Fig. 2.3a, b).

We performed the calculation until 12 h after the earthquake and output the velocities every 0.5 s within the radar coverage. Tsunami-induced velocity vectors $\boldsymbol{V}_{\mathrm{tsu}}(m, t)$ at each cell along beam 04 were linearly interpolated from the simulated velocities, where m (m = 1, …, 64; see Fig. 2.1c) is the cell number along beam 04 and t is the time. Radial velocities $v_{\mathrm{tsu}}(m, t)$ were then created by calculating the inner product between $\boldsymbol{V}_{\mathrm{tsu}}(m, t)$ and the unit vector along beam 04. The maximum radial velocities and the maximum tsunami heights at all cells were generated by the large slip, which appeared in the passage of the first wave. The maximum radial velocities at cells 10, 20, and 30 were approximately 120, 50, and 20 cm/s, respectively (Fig. 2.3a, b). The dominant period of the first wave of the tsunami was approximately 60 min.

2.2.3 Virtual tsunami observation experiments

(1) Production of virtually observed tsunami-induced radial velocities

In the experiments, we created the receiving signals that would have been observed along beam 04 if the tsunami had occurred in February 2014. First, we calculated Doppler frequencies associated with the simulated tsunami velocities, which include

neither background noise (BGN) nor BGC information. These ideal signals were calculated by using Eqs. (4) and (5) (Gurgel et al. 2011):

$$\Theta(m,t) = a_x \exp\left(2\pi j \int_{t_0}^{t} f_{\text{tsu}}(m,\tau)\, d\tau \right), \tag{4}$$

$$f_{\text{tsu}}(m, t) = 2 f_0 \, v_{\text{tsu}}(m, t) / c, \tag{5}$$

where m is the cell number (m = 1, …, 64), t_0 is the time when the tsunami occurred, f_{tsu} is the additional Doppler frequency shift due to v_{tsu}, j is the imaginary unit, f_0 is the transmitting frequency of HF radar, c is the propagation speed of radio waves, a_x is an arbitrary amplitude and is set to 1, and $d\tau$ is the output interval of the simulated velocities.

Considering the rather simple bottom topography along beam 04 (Fig. 2.1a, 2c), we assumed that the simulated tsunami-induced current $v_{\text{tsu}}(m, t)$ could be linearly superimposed on the observed BGCs at each cell. To synthesize the receiving signals measured during the tsunami events, the artificial signals $\Theta(m, t)$ were superimposed on the actual receiving signals $S(m, t)$ along beam 04 measured during February 2014 by calculating the Hadamard product:

$$X(m, t) = S(m, t) \otimes \Theta(m, t). \tag{6}$$

$S(m, t)$ represents the signals associated with BGCs including BGN, and thus $X(m, t)$ represents the signals associated with tsunamis and BGCs including BGN. The synthesized method would not be completely valid in areas where strong nonlinearity exists such as near the coast line, in and around narrow straits and behind capes. Since HF radar observation had failed due to intermittent system troubles in 33/660 tsunami event cases, we eventually synthesized the receiving signals in the other 627 cases. Note that the ideal signals were identical in all 627 cases for each cell.

We then calculated Doppler spectra at 64 range cells every 1 min by performing a 256-sample (128 s) FFT overlapping by 128 samples (64 s), resulting in a velocity resolution of 4.78 cm/s. Figure 2.4a–c shows examples of the calculated Doppler spectra of ideal, observed, and synthetic signals, respectively: Fig. 2.4a shows the Doppler spectra obtained 13 min after the tsunami event; Fig. 2.4b shows the Doppler spectra actually observed at 06:13 on February 3, 2014; Fig. 2.4c shows the Doppler spectra which would have been obtained 13 min after the earthquake if the tsunami had been excited at 06:00 on February 3, 2014.

We next calculated the observed and synthesized radial velocities from the corresponding Doppler spectra every 1 min (Fig. 2.5a). Since the dominant period of the first wave of the simulated tsunami was approximately 60 min, we decomposed these

radial velocities into two components by using a 60-min moving average and analyzed the shorter-period components $v_{obs}(m, t)$ and $v_{vt}(m, t)$: $v_{obs}(m, t)$ is the observed radial velocity which contains information of shorter-period BGC physics and BGN; $v_{vt}(m, t)$ is the synthesized radial velocity which additionally contains the tsunami-induced current.

(2) Tsunami detection method

Assuming that the fault model case 3-induced tsunami occurred at 00:00 on April 5, 2014 and using the receiving signals of the Mihama site, Fuji et al. (2015) conducted a virtual tsunami experiment, and revealed that (1) when Δr (the distance between the two points along beam 04) $\geq$ 3.0 km, the shorter-period radial velocities at the two points were almost uncorrelated before tsunami arrival, and (2) cross-correlation increased significantly 60 min after tsunami arrival. Following Fuji et al. (2015), here we detect the tsunami based on the temporal change in the cross-correlation of the radial velocities at the two points spaced 3.0 km apart (Δr = 3 km) along beam 04.

Figure 2.6 illustrates the detection method. The tsunami arrival time ($t = t_a$) in each cell was defined as the time when the radial velocity calculated by the numerical tsunami model $v_{tsu}(m, t)$ first exceeds ± 4.78 cm/s, which is identical to the velocity

resolution of the radar. The time of tsunami detection t_d is 60 min after the arrival of the first tsunami wave (Fig. 2.6a).

Let $t_n = n\Delta t$ (Δt = 1 min, n = 360, 361, …, 39,900) be the elapsed time in minutes from 00:00 on February 1, 2014. Cross-correlations $\mathrm{cor}_{\mathrm{obs}}(m, t_n)$, $\mathrm{cor}_{\mathrm{vt}}(m, t_n)$ between the two points were respectively calculated from the combinations of $v_{\mathrm{obs}}(m-2, t_n)$, $v_{\mathrm{obs}}(m, t_n)$ and $v_{\mathrm{vt}}(m-2, t_n)$, $v_{\mathrm{vt}}(m, t_n)$:

$$\mathrm{cor}_{\mathrm{obs,vt}}(m,t_n)=\frac{\sum_{k=n-60}^{n}\left(v_{\mathrm{obs,vt}}(m-2,t_k)-\overline{v_{\mathrm{obs,vt}}(m-2)}\right)\left(v_{\mathrm{obs,vt}}(m,t_k)-\overline{v_{\mathrm{obs,vt}}(m)}\right)}{\sqrt{\sum_{k=n-60}^{n}\left(v_{\mathrm{obs,vt}}(m-2,t_k)-\overline{v_{\mathrm{obs,vt}}(m-2)}\right)^2}\sqrt{\sum_{k=n-60}^{n}\left(v_{\mathrm{obs,vt}}(m,t_k)-\overline{v_{\mathrm{obs,vt}}(m)}\right)^2}}, \quad (7)$$

where the overbar denotes the 60-min time average during the period from $t = t_{n-60}$ to $t = t_n$.

$\mathrm{cor}_{\mathrm{obs}}(m, t_n)$ was calculated every 1 min from 06:00 on February 1, 2014 to 17:00 on February 28, 2014, then was resampled every 60 min. In total, a time series of 627 cross-correlations at each cell was obtained except the time when the radar observation had failed. Then, a histogram of the cross-correlation $P[\mathrm{cor}_{\mathrm{obs}}(m, t_n)]$ was calculated by using resampled $\mathrm{cor}_{\mathrm{obs}}(m, t_n)$. As an example, Fig. 2.6b shows $P[\mathrm{cor}_{\mathrm{obs}}(12, t_n)]$. The frequency distribution can be well-approximated by a normal distribution (mean μ,

standard deviation σ). The radial velocities at the two points were generally uncorrelated ($\mu \approx 0$) without tsunami events.

$\mathrm{cor}_{\mathrm{vt}}(m, t_n)$ was calculated every 1 min for 627 synthesized signals at each cell. Fig. 2.6a shows the time series of $v_{\mathrm{vt}}(10, t_n)$, $v_{\mathrm{vt}}(12, t_n)$ and $\mathrm{cor}_{\mathrm{vt}}(12, t_n)$ for the case in which the tsunami occurred at 06:00 on February 7, 2014. Negative velocities emerged before $t = t_{\mathrm{a}}$, which is due to use of the 60-min moving average for extracting the shorter-period components [$v_{\mathrm{vt}}(m, t_n)$] from the synthesized velocities. Effects of the decomposition by using the moving average on the extraction of tsunami velocities will be discussed in Subsection 2.3.2 .

We detected the tsunami by using $\mathrm{cor}_{\mathrm{vt}}(m, t_n)$ at $t_n = t_{\mathrm{d}}$ and $P[\mathrm{cor}_{\mathrm{obs}}(m, t_n)]$ approximated by a normal distribution (Fig. 2.6b). Here, we define $F(m)$ as a significance function representing the significance of the difference of cross-correlation before and after the arrival of the tsunami. When $\mathrm{cor}_{\mathrm{vt}}(m, t_n)$ at t_{d} was ranked in the top 1% of $P[\mathrm{cor}_{\mathrm{obs}}(m, t_n)]$, we set $F(m) = 1$, otherwise $F(m) = 0$. Furthermore, we define $TD(m)$—a tsunami detection factor—as follows (see also Fig. 2.5b):

$$\mathrm{TD}(m) = F(m-2) \cdot F(m-1) \cdot F(m). \tag{8}$$

In total, 627 TD(m) values at each cell were calculated. Tsunami detection was finally judged based on TD(m): when TD(m) = 1, we judged that the tsunami was detected at cell m. The use of information in adjacent range cells is similar to the method developed by Lipa et al. (2012a, b).

The tsunami detection was performed for each cell in all 627 cases and the monthly detection probability for each cell was calculated. In general, tsunami-induced current velocities are rather small beyond the continental shelf. Even within the offshore cells where $v_{\mathrm{tsu}}(m, t_n) \ll v_{\mathrm{obs}}(m, t_n)$—namely $v_{\mathrm{vt}}(m, t_n) \approx v_{\mathrm{obs}}(m, t_n)$, and thus the HF radar would not detect the tsunami—$F(m)$ will become 1 with a probability of 1%. Therefore, we used cross-correlations in three adjacent range cells to avoid misdetection of tsunami. The possibility of misdetection significantly decreases even at the offshore cells by using TD(m) instead of $F(m)$.

From the definition, 60-min averages of the shorter-period component of observed velocity are equal to zero, that is, $\overline{v_{\mathrm{obs}}(m,t_n)} = 0$. Since the simulated tsunami first wave has a dominant period of about 60 min, $\overline{v_{\mathrm{tsu}}(m,t_n)} \approx 0$. Hence, $\overline{v_{\mathrm{vt}}(m,t_n)} \approx \overline{v_{\mathrm{obs}}(m,t_n)} + \overline{v_{\mathrm{tsu}}(m,t_n)} \approx 0$. In addition, the following approximations hold, since the correlations of independent velocities are generally zero:

$$\sum_{k=n-60}^{n} v_{\mathrm{obs}}\left(m-2,t_k\right) v_{\mathrm{obs}}\left(m,t_k\right) \approx 0 \quad , \tag{9}$$

$$\sum_{k=n-60}^{n} v_{\mathrm{obs,tsu}}\left(m-2,t_k\right) v_{\mathrm{tsu,obs}}\left(m,t_k\right) \approx 0 \quad . \tag{10}$$

Taking into account that $v_{\mathrm{obs}}(m-2,\, t_n)$ and $v_{\mathrm{obs}}(m,\, t_n)$ are of the same order (Fig. 2.6a) and the spatial scale of the tsunami wave is much larger than the distance between cell $m-2$ and cell m (Fig. 2.3a, Fig. 2.6a),

$$\sum_{k=n-60}^{n} v_{\mathrm{obs}}^2\left(m-2,t_k\right) \approx \sum_{k=n-60}^{n} v_{\mathrm{obs}}^2\left(m,t_k\right) \quad , \tag{11}$$

$$\sum_{k=n-60}^{n} v_{\mathrm{tsu}}^2\left(m-2,t_k\right) \approx \sum_{k=n-60}^{n} v_{\mathrm{tsu}}^2\left(m,t_k\right) \quad . \tag{12}$$

From these approximations, the cross-correlation $\mathrm{cor}_{\mathrm{vt}}(m,\, t_n)$ at $t_n = t_{\mathrm{d}}$ of Eq. (7) is approximated by:

$$\mathrm{cor}_{\mathrm{vt}}\left(m,t_n\right) \approx \frac{\sum_{k=n-60}^{n} v_{\mathrm{tsu}}^2\left(m,t_k\right)}{\sum_{k=n-60}^{n}\left(v_{\mathrm{obs}}^2\left(m,t_k\right)+v_{\mathrm{tsu}}^2\left(m,t_k\right)\right)} = \frac{1}{\frac{1}{E_{\mathrm{ratio}}\left(m,t_n\right)}+1} \quad , \tag{13}$$

where

$$E_{\mathrm{ratio}}(m,t_n)=\frac{\sum_{k=n-60}^{n} v_{\mathrm{tsu}}^2(m,t_k)}{\sum_{k=n-60}^{n} v_{\mathrm{obs}}^2(m,t_k)}. \tag{14}$$

$E_{\mathrm{ratio}}(m, t_n)$ represents the kinetic energy ratio between tsunami-induced velocity $v_{\mathrm{tsu}}(m, t_n)$ and $v_{\mathrm{obs}}(m, t_n)$, which includes the shorter-period component of BGCs and BGN. Larger BGCs and/or larger BGN result in a smaller $E_{\mathrm{ratio}}(m, t_n)$. Hence:

$$\mathrm{cor}_{\mathrm{vt}}(m,t_n)\sim\begin{cases}1 & \text{for} \quad E_{\mathrm{ratio}}>>1\\ 0 & \text{for} \quad E_{\mathrm{ratio}}<<1\end{cases}. \tag{15}$$

Cross-correlation $\mathrm{cor}_{\mathrm{vt}}(m, t_n)$ depends primarily on the energy ratio. Basically, in the onshore–offshore direction, the energy ratio is small beyond the continental shelf where tsunami-induced current velocities are rather small (Fig. 2.3b). At cell m, the kinetic energy of $v_{\mathrm{tsu}}(m, t_n)$ does not change in this study and hence the energy ratio varies in accordance with temporal variations of $v_{\mathrm{obs}}(m, t_n)$.

We examined the degree of coincidence between $v_{\mathrm{vt}}(m, t_n)$ and $v_{\mathrm{tsu}}(m, t_n)$ by using variance reduction (VR; eg., Cummins et al. 2009) defined by:

$$\mathrm{VR}(m)=\left\{1-\frac{\sum_{k=n}^{n+60}\left(v_{\mathrm{vt}}(m,t_n)-v_{\mathrm{tsu}}(m,t_n)\right)^2}{\sum_{k=n}^{n+60}\left(v_{\mathrm{tsu}}(m,t_n)\right)^2}\right\}\times 100(\%) \tag{16}$$

.

The National Research Institute for Earth Science and Disaster Resilience (NIED; http://www.fnet.bosai.go.jp/event/dreger.php?LANG=en) evaluates the quality of the value regarding earthquake moment tensor analysis: 100% is best, more than 80% is good, 50% is fairly good, less than 20% is not good. This allows us to understand how accurately we can measure the variability of tsunami velocity in ranges where the tsunami would have been detected.

2.3 Results and discussion

2.3.1 Tsunami detection probability on and beyond the continental shelf

This study conditionally examined detection probability by using 1-month observation signals on the Mihama coast in February 2014 and assuming a scenario of the fault model case 3 of a Nankai Trough earthquake. Fig. 2.7 shows onshore-offshore distributions of the tsunami detection probability in February 2014, the monthly average energy ratio, the maximum tsunami-induced radial velocity, and the water depth along beam 04. The combination of the present detection method and the NJRC radar system shows a high detection probability of 100% within cells 7–20, and around 90% at cell 25. The probability decreased to 25% at cell 30 and decreased gradually far offshore, approaching 0% at cell 50 (Fig. 2.7). The probability decreased significantly

in cells 20–30 over the shelf slope. The maximum tsunami-induced velocity varies from 53 to 19 cm/s and the energy ratio decreased significantly from about 30 to 1 over the shelf slope, which led to a significant decrease in cross-correlation, and hence in the monthly detection probability.

The probability stayed at over 90% when $E_{ratio} > 5$ from cell 6 to cell 24 (offshore distance: 9 km $\leq L \leq$ 36 km and water depth: 50 m $< h <$ 600 m) and stayed at around 50% when $E_{ratio} \approx 1$ at cell 28 (L = 42 km, h = 1200 m). For the cells near the coast, the radar could not accurately measure the surface currents due to the limitations of our radar system specifications. As a result, the probability of the tsunami detection becomes zero from cell 1 to cell 4. However, this will not cause a serious problem since the detection probability offshore is the key for tsunami mitigation. The tsunami propagates approximately along beam 04. The probability for a distance L along different beams would decrease compared with the above result along beam 04, because the energy ratios along the different beams would decrease due to the difference of the directions between the radar beams and tsunami propagation.

Figure 2.8a shows the time–distance diagram of the tsunami detection results along beam 04. The maximum detection distance offshore, as an example, varied greatly from cell 20 (L = 30 km) at 14:00 on February 27 to cell 48 (L = 72 km) at 01:00 on February

8. The variability of the maximum detection distance corresponds well with that of the energy ratio (Fig. 2.8b) as predicted by Eqs. (13) and (14). Temporal variations of the energy ratio and TD(m) at cell 25 are extracted in Fig. 2.8c. The tsunami could not be detected by the combination of the method and the NJRC radar system when $E_{\mathrm{ratio}}(25, t_{\mathrm{d}}) < 0.5$.

We divided the energy ratio ranging between 0.1 and 10.0 of the 627 cases for 64 range cells (N = 40,128) by 0.1 and calculated the detection probability for each interval (Fig. 2.9). The probability of tsunami detection was around 50% when $E_{\mathrm{ratio}}(m, t_{\mathrm{d}}) = 1$ and was larger than 80% when $E_{\mathrm{ratio}}(m, t_{\mathrm{d}}) \geq 2$. This close relationship demonstrates that calculations of the energy ratio using tsunami simulations and the HF radar observations under the condition of no tsunami for the regions of interest allow us to roughly estimate the tsunami detection probability without conducting the virtual tsunami observation experiments.

We estimated the influence of a moving average period on the tsunami detection probability. Figure 2.10 shows a comparison of the longer-period components of synthetic velocities (thin line) and of observed velocities (thick line) at cells 10 (red), 20 (blue), and 30 (black) assuming the tsunami was excited at 06:00 on February 7, 2014. The hatched area indicates errors of the synthetic velocities from 06:00 to 07:00

obtained by using a 60-min moving average. The errors lead to underestimation of $v_{vt}(m, t_n)$ resulting in decreases in tsunami energy. The total energy of $v_{vt}(m, t_n)$ from 06:00 to 07:00 at these cells was underestimated by 3.5% (cell 10), 3.5% (cell 20), and 17.5% (cell 30) due to the errors in extraction of the longer-period components (Table 2.2). By correcting the underestimation of the total energy of $v_{vt}(m, t_n)$, we inferred from Fig. 2.9 (Table 2.2) that the detection probability at cell 30 would increase by around 10%, while those at cells 10 and 20 remain at 100%. Figure 2.9 suggests that for cells with smaller energy ratio s (i.e., 0.1–2.0), accurate extraction of the longer-period component leads to an increase of the ratio, which would result in an improvement of the detection probability.

Figure 2.8d shows the time–distance diagram of VR(m), which is almost 80% in ranges where the tsunami detection succeeded and less than 10% in ranges where the detection failed. VR(m) is in good agreement with the energy ratio (Fig. 2.8a). From the comparison of VR(m) and the energy ratio shown in Fig. 2.11, it is clear that dependence of VR(m) on the energy ratio is completely different between detection results (detected and not detected). When the tsunami detection succeeded VR(m) was almost 80% for $E_{ratio} > 5$, and the corresponding detection probability was 90%. Meanwhile, when the tsunami detection failed, VR(m) ranged from 0 to 80%. This

suggests that velocity variability of the detected tsunami can be quantitatively used for tsunami mitigation, such as to check the category of the tsunami warning issued by the JMA, estimate tsunami height along the coast, and estimate tsunami source based on the inversion method (Satake 1987; Tsushima et al. 2009, 2011, 2012; Fuji et al. 2013), and thus specify areas subject to devastating damage by numerical simulation, in addition to detection of the tsunami. In the next Subsection 2.3.2 we examine tsunami height inferred from offshore radar velocities in a case study.

2.3.2 Nearshore tsunami heights predicted from offshore velocity measurements

The JMA issues the first warning 3 min after the occurrence of an earthquake based on a tsunami forecast database, which is created by using the linear long-wave calculation and Green's law. Around 100,000 scenarios are calculated in advance. First, tsunami heights at around 15 km offshore are calculated by using a linear long-wave model, then the tsunami heights near the coast are estimated from the offshore tsunami heights based on Green's law, which saves time and provides enough lead time for evacuation. However, the first warning of the 2011 Tohoku-Oki earthquake underestimated the tsunami height due to saturation of the magnitude calculated by seismometer measurements. It is crucial to avoid underestimation, which is also a major

concern for a Nankai Trough earthquake. In this study, we calculated the tsunami heights near the coast based on the offshore tsunami velocity measurements and the same method of the JMA to validate whether or not the NJRC radar system has the potential to check the categories of tsunami warning issued by the JMA.

Figure 2.12 shows an example of the time series of $v_{vt}(m, t_n)$ and $v_{tsu}(m, t_n)$ at cells 10, 20, and 30 assuming the tsunami was excited at 06:00 on February 7, 2014. The maximum detection distance was cell 32 (L = 48 km) for this case. Overall, $v_{vt}(m, t_n)$ is in good agreement with $v_{tsu}(m, t_n)$ at cells 10, 20, and 30. The large slip-induced maximum velocity, which appeared at the second local peak with a time scale of less than 5 min in the first tsunami wave, has been observed at cells 10 and 20 from the virtual tsunami observation experiment. This is of great importance, because the maximum velocity is associated with the maximum tsunami height.

We converted the radial velocities at cells 10, 20, and 30 to tsunami heights by the formula: $\eta_{vt}(m,t_n) = \sqrt{h/g}\, v_{vt}(m,t_n)$. Then, the tsunami heights near the coast at cell 1 (h = 10 m) on beam 04 were estimated based on Green's law: $\eta_{coast} = (h(m)/h(1))^{1/4} \eta_{vt}(m,t)$. The gaps in the maximum velocities between the true values $v_{tsu}(m, t_n)$ and virtually observed values $v_{vt}(m, t_n)$ at cells 10 (h = 80 m), 20 (h = 270 m), and 30 (h = 1350 m) were approximately −12, −8, and +7 cm/s,

respectively. The gaps cause estimation errors of the maximum tsunami height by −0.34, −0.42, and +0.82 m at these cells. Based on Green's law, resultant estimation errors of the maximum tsunami height near the coast (h = 10 m) were respectively −0.58, −0.96, and +2.80 m (Table 2.3).

The simulated tsunami height (true value) was 6.8 m near the coast where h = 10 m. The height corresponds to a JMA "Major Tsunami Warning" category (Table 2.3). By using $v_{vt}(m, t_n)$ at cells 10, 20, and 30 based on Green's law, the nearshore tsunami heights were predicted to be 6.01 m from cell 10, 5.63 m from cell 20, and 9.38 m from cell 30 (Table 2.3). All the predicted heights correspond to the "Major Tsunami Warning" category. Thus, the NJRC radar system had the potential to validate the JMA tsunami warning in this case, where the tsunami was assumed to be excited at 06:00 on February 7, 2014.

Figure 2.10 shows that the synthetic velocities started to deviate from the observed velocities about 30 min prior to the tsunami arrival and eventually overestimated the BGCs by about 20, 10, and 5 cm/s. This was because we decomposed the radial velocities by using a 60-min moving average. The overestimations of the longer-period components at cells 10 and 20 led to underestimation of the shorter-period components,

which resulted in the underestimation of the maximum tsunami height near the coast (Table 2.3).

In Japan, in addition to detecting tsunami arrival offshore, it is important to check the category of tsunami warning issued by the JMA. For this reason, in real-time detection, tsunami-induced current components should be extracted from the observed velocities by using a high-pass filter (e.g., 60-min moving average in this study). However, tsunami period, which generally becomes longer as M_w becomes greater, cannot be obtained in real time. The dominant period of the tsunamis caused by the M_w 9.0 2011 Tohoku-Oki earthquake was estimated to be approximately 30–60 min (e.g., Hinata et al. 2011). In the actual real-time detection, we consider using a high-pass filter with longer window size, such as 120-min moving average, which should be used in preparation for huge tsunamis. When using the moving average to extract the tsunami-induced velocities, BGCs over the time corresponding to the last half of the filter window cannot be obtained in real time; hence, the estimation of BGCs by using (for example) a linear extrapolation or autoregressive (AR) model (e.g., Fuji et al. 2015) will also be required.

2.3.3 Probabilistic analysis on nearshore tsunami height using one-month data

In the previous Subsection 2.3.2 , we found that the tsunami height near the coast inferred from offshore velocities by radar at cells 10, 20, and 30 assuming the tsunami was excited at 06:00 on February 7, 2014 sufficiently corresponded to the JMA “Major Tsunami Warning” category. In this subsection, we demonstrate the applicability of the method for checking the JMA “Major Tsunami Warning” category using one-month offshore velocities by estimating nearshore tsunami height considering estimation error.

Figure 2.12 shows the apparent time lag of the maximum velocities of the tsunami first wave between $v_{\mathrm{tsu}}(m, t_n)$ and $v_{\mathrm{vt}}(m, t_n)$ at cell 30. This indicates that fluctuation of time lag increases offshore and temporally varies in other cases. Hence, we also considered time lag to evaluate nearshore tsunami height. Figure 2.13a shows the time–distance diagram of tsunami propagation. The green line represents a theoretical curve obtained by back-calculating propagation from the speed of the linear long-wave starting from the time of tsunami arrival at the coast. This line, defined as the “theoretical tsunami wavefront of linear long-wave”, means the time of manifestation of tsunami-induced velocity in each cell. The blue line represents the time of manifestation of the maximum velocities of the tsunami first wave. The color scale bar indicates

probability concerning time lag P[lag(m)] which satisfies that the lag is less than 2 min (|lag(m)| ≤ 2 min). P[lag(m)] is over 80% in ranges from cell 3 to 20.

Figure 2.13b shows the distribution of the maximum tsunami height near the coast, which was estimated from offshore simulated velocity, to the distance where the velocity is used to estimate the height (blue line). The predicted height significantly decreases at cell 6. In ranges where the predicted height is over 3 m including estimation error, which corresponds to the JMA "Major Tsunami Warning" category, the predicted nearshore tsunami heights are adequate. The color scale bar indicates probability concerning nearshore height P[error(m)] which satisfies that the estimation error of the nearshore height predicted by $v_{tsu}(m, t_n)$ and $v_{vt}(m, t_n)$ is less than 2 m (|error(m)| ≤ 2 m). P[error(m)] is over 80% in ranges from cell 7 to 25. Since nearshore height predicted by numerical simulation is 6.8 m (Table 2.3), the height considering the estimation error also corresponds to the JMA "Major Tsunami Warning" category.

Figure 2.13c shows the probability concerning time lag P[lag(m)] (solid black), predicted nearshore tsunami height P[error(m)] (dashed black), and the joint probability P[lag, error(m)] (solid red). The light blue line shows the tsunami detection probability (Fig. 2.7). P[lag, error(m)] is in accordance with the detection probability. In particular, both probabilities are over 95% in ranges from cell 8 to 21 on the continental shelf.

Again, the decrease of the probability for the cell near the coast is due to our radar system specifications (Subsection 2.3.1); both probabilities significantly decrease beyond the continental shelf edge (cell 20). P[lag, error(m)] is lower than the detection probability by around 20 points in ranges from cell 20 to 30. Thus, the detection method using cross-correlation has great potential for evaluating nearshore tsunami height to mitigate tsunami impact.

2.3.4 Signal, noise and signal-to-noise ratio (SNR) variability

The possibility of tsunami detection primarily depends on the energy ratio between $v_{\mathrm{tsu}}(m, t_n)$ and $v_{\mathrm{obs}}(m, t_n)$ at $t_n = t_{\mathrm{d}}$ in our method. $v_{\mathrm{tsu}}(m, t_n)$ was identical for each cell in the 627 cases of virtual tsunami observation experiments. Hence, the energy ratio changed temporally in accordance with the variations of $v_{\mathrm{obs}}(m, t_n)$, which include information of shorter-period BGCs and BGN. Figure 2.14 shows the scatter plot of five cell-averaged SNR values in cells 21–25, cells 26–30, cells 31–35, and cells 36–40 and energy ratio obtained over the continental shelf slope, where the detection probability significantly decreases (Fig. 2.7). We calculated SNR as follows:

$$\mathrm{SNR} = 10 \log_{10} \frac{\max\left\{P_{\mathrm{Sp}}, P_{\mathrm{Sm}}\right\}}{\min\left\{P_{\mathrm{Np}}, P_{\mathrm{Nm}}\right\}}, \tag{17}$$

where P_{Sp} and P_{Sm} are the energy of the first-order spectral peaks in the positive and negative frequency regions, respectively. We calculated P_{Np} and P_{Nm} as the averaged energy in the Doppler frequency bands of $-1.0 \leq f \leq -0.9$ and $0.9 \leq f \leq 1.0$, respectively. We calculated SNR in order to maximize the value and thus examine the maximum detection distance. For this reason, we used max at the numerator and min at the denominator.

The energy ratio was significantly ($P < 0.001$) but not strongly correlated with SNR with correlation coefficients of 0.47 (cells 21–25), 0.57 (cells 26–30), 0.64 (cells 31–35), and 0.59 (cells 36–40), suggesting that the energy ratio varied in accordance with the variations of SNR and also of the shorter-period BGCs as mentioned in Subsection 2.2.3 . We could not obtain the BGC velocity measurement data, such as by an acoustic Doppler current profiler. Hence, we examined the effects of SNR variability on the tsunami detection and factors generating the SNR variability.

Overall, the temporal variations of receiving signals and SNR correspond well to each other (Fig. 2.15a, b, d). As an example, signals were as high as about −50 dBm in the nighttime on February 01, 09–10, 16–17, and 24–25, 2014, and were as low as −80 dBm in the daytime on February 27 at cell 25 (Fig. 2.15d). Diurnal variations of receiving signals were not as apparent as those of SNR (Fig. 2.15d). The signals and the

significant wave heights (Fig. 2.15e) observed by the Wakayama-Nanseioki GPS wave gauge (Fig. 2.1a) showed a strong inverse correlation ($r = -0.72$, $P < 0.001$; Fig. 2.16).

Barrick (1971) demonstrated that the normalized effective surface impedance, which is largely affected by the ocean wave heights, significantly affects the propagation loss of HF radar transmission waves and the loss increases for rougher seas and longer propagation distances. Based on his Fig. 2.10 and Fig. 2.12, the propagation loss of the waves 50 km offshore at 20 (50) MHz was approximately less than 1 (2) dB at a 5-knot wind and 10 (9) dB at a 30-knot wind. Therefore, smaller signals observed on February 15 and 27 were mainly due to attenuation by the scattering of transmitting and receiving signals with the growth in height of sea surface waves.

From the comparison between Fig. 2.8 and Fig. 2.15, higher surface waves decreased the receiving signals of the radar and thus SNR, resulting in a decrease of the maximum tsunami detection distance, e.g., on February 15 and 27, while lower waves increased the receiving signals and SNR but did not necessarily increase the detection distance, e.g., on February 09–10, 16–17, and 24–25. This again suggests that the energy ratio depends not only on SNR but also on the variations of shorter-period BGC physics. Figure 2.17 indicates that the maximum detection distance is uncorrelated to the significant wave height. The distance is up to around cell 20 for wave heights higher

than 4 m. In contrast, the distance varies from around cell 20 to cell 50 for wave heights lower than 4 m.

In contrast, the diurnal variations were predominant in the noise variability (Fig. 2.15c, d). Generally, the ionospheric critical frequency has an apparent diurnal variation, i.e., minimum in early morning and midnight, and maximum at noon (e.g., Ishii 2009). Transmitting and receiving waves of the HF radar (24.515 MHz) are reflected by the F layer. We examined the temporal variability of the critical frequency at Kokubunji (35°42'N, 139°29'E, Fig. 2.1b) for vertical soundings using the ionosphere observations conducted by NICT (http://wdc.nict.go.jp/cgi-bin/ionog/manualfv). The diurnally averaged critical frequency in February 2014 showed an apparent diurnal fluctuation of 3.59 MHz (minimal) at 05:00 and 12.20 MHz (maximal) at 12:00.

We additionally examined the temporal variability for oblique soundings [transmitting station: Kokubunji, receiving station: Okinawa (26°40’N, 128°09’E), Fig. 2.1b)] based on their contour plots published on their website (http://wdc.nict.go.jp/IONO/). The ionospheric reflections occurred in a frequency band including 24.515 MHz at around 3 00 km above the surface during approximately 8:00–17:00 in February 2014 (http://wdc.nict.go.jp/IONO/). The Mihama coast is midway between Kokubunji and Okinawa stations. This suggests that noises at a distance far

from our HF radar site reflected by the F2 layer could interfere with the HF radar receiving signals. In addition to the reflection, human activities increasing in the daytime would be a cause of the diurnal variations of the receiving noise.

We calculated the diurnal variation of the detection probability by applying ensemble averaging except for February 15 and 27 when extremely large wave heights were observed (Fig. 2.18). The range with 80% detection probability varied corresponding to the diurnal noise variability. The detection distance with 80% probability was as far as cell 28 in the nighttime, and as near as cell 25 at 16:00. The averaged maximum detection distance diurnally varied by more than 10%.

2.3.5 Application of tsunami detection method to other tsunamis

For the 2011 Japan tsunami, Lipa et al. (2012a) succeeded in detecting the tsunami arrival at shallow water regions ($h < 200$ m) on the eastern coast of Hokkaido, Japan and the western coast of the USA (Oregon and California). They detected the tsunami arrival by using averaged velocities in three adjacent alongshore bands: 6–8, 8–10, and 10–12 km in Hokkaido; 8–10, 10–12, and 12–14 km in Oregon and California. We read the time series of the velocities within the 10–12-km band in Hokkaido and the 12–14-km band in Oregon and California from their figures (Figs. 5c, 8c, 9c), and identified

the amplitudes of the variability before (after) the passage of the tsunami as 2 cm/s (7 cm/s), 3 cm/s (7 cm/s), and 4 cm/s (9 cm/s), and eventually found the energy ratios were 12.3, 5.4, and 5.1. The possibility of tsunami detection by our method primarily depends on the energy ratio. Tsunami energies off Hokkaido, Oregon and California coasts include the effects of tsunami magnitude and local bottom topography on tsunami velocity of the 2011 Japan tsunami. BGC energies off Hokkaido, Oregon and California coasts include an effect of BGN at each radar site. Thus, from the relationship obtained in Fig. 2.7, we considered that the combination of the present model and the NJRC radar system would have detected the tsunami arrival with a probability of over 90% 10–12 km offshore from the Hokkaido coast and 12–14 km offshore from the US coasts.

For the 2012 Indonesian tsunami, Lipa et al. (2012b) succeeded in detecting the tsunami arrival off Padang on the west coast of Sumatra and off Hut Bay on the Andaman Islands, but failed off Port Blair on the Andaman Islands due to weak correlation of velocity peaks in the adjacent bands. They used the averaged velocities in three or four adjacent bands: 0–2, 2–4, and 4–6 km in Padang; 6–12, 12–18, and 18–24 km in Hut Bay; 0–6, 6–12, 12–18, and 18–24 km in Port Blair. Again, we read the velocity variability within the range of 4–6 km in Padang, 18–24 km in Hut Bay, and

18–24 km in Port Blair from their figures (Figs. 3c, 5c, 7c). The amplitudes before (after) the tsunami arrival were 4 cm/s (10 cm/s), 4 cm/s (8 cm/s), and 5 cm/s (13 cm/s), respectively, and resultant energy ratios were 6.3, 4.0, and 6.8. Thus, as in the above example regarding the 2011 Japan tsunami, we considered that we would have detected the tsunami arrival with a detection probability of over 90% in Padang and Port Blair, and 85–90% in Hut Bay.

Gurgel et al. (2011) judged tsunami arrival by using the OS-CFAR algorithm (Rohling 1983). They successfully detected the tsunami arrival within the offshore ranges where $h < 160$ m. Based on their figures (Figs. 10, 11), the maximum radial velocities of tsunami-induced current and of the BGCs were, respectively, about 100 and 10 cm/s within the ranges, resulting in the energy ratio of about 100. Thus, the tsunami would have been detected with a probability of almost 100% around the continental shelf edge. Furthermore, with these BGCs, much smaller tsunamis with a maximum velocity of around 22 cm/s (the corresponding energy ratio is 5) are detectable with a probability of 90%.

2.4 Summary

In this chapter, we examined the tsunami detection performance of the present method combined with the NJRC radar system through *a posteriori* analysis based on virtual tsunami observation experiments by using receiving signals of the NJRC high-frequency radar during February 2014 installed on the Mihama coast, Japan and numerically simulated velocities induced by a M_w 9.0 Nankai Trough earthquake. In the experiments, the artificial signals associated with the simulated tsunami velocities were superimposed on the receiving signals of the radar by the method developed by Gurgel et al. (2011), and the radial velocities were calculated from the synthesized signals by the FFT. Tsunami arrival was then detected based on the temporal change in the cross-correlation of the radial velocities, before and after tsunami arrival, between two range cells 3 km apart along beam 04.

We found that the possibility of tsunami detection primarily depends on the kinetic energy ratio between tsunami and shorter-period BGC velocities. In the onshore–offshore direction, the monthly average detection probability is over 90% when the energy ratio exceeds 5 (offshore distance: $9\ \mathrm{km} \leq L \leq 36\ \mathrm{km}$ and water depth: $50\ \mathrm{m} < h < 600\ \mathrm{m}$) and is about 50% when the energy ratio is approximately 1 ($L = 42$ km, $h = 1200$ m). The probability reduced over the continental shelf slope with

decreasing tsunami-induced velocities. The maximum detection distances obtained hourly in this study (Fig. 2.8a) by using 60-min information of the measured tsunami-induced velocities after tsunami arrival could be used as a "target value" for real-time detection, since only (for example) 2–5 min of information would be available in real-time tsunami detection, which will lead to a reduction in the maximum detection distance.

For a certain range cell on the radar beam, the energy ratio temporally varied in accordance with the variations of ocean surface wave height, ionospheric electron density and also with the shorter-period BGC physics. From statistical analyses of the Wakayama-Nanseioki GPS wave gauge (not shown here), significant wave heights are smaller from spring to summer, that is to say, the receiving signals would be more intense in this season. Meanwhile, the ionospheric electron density of the F2 layer generally becomes greater in the season, which would lead to greater receiving noise in the daytime.

Fuji et al. (2015) examined tsunami detection assuming that the tsunami occurred at 00:00 April 5, 2014, and reported that the maximum detection distance was 52.5 km (cell 35). In this study, the monthly average maximum detection distance with a probability of 100% is 30.0 km (cell 20). The decrease of detection distance by 22.5 km

(15 cells) may be caused by higher ocean surface waves in February, in spite of the weakening of the ionospheric electron density of the F2 layer. The monthly average significant wave height in February was the highest of 2014. The dependence of the detection distance on the wave heights indicates that detection probability in other seasons should be examined.

In actuality, the energy ratio also varies depending on the tsunami magnitude. When a weaker (greater) tsunami occurs, the energy ratio becomes small (large) and the maximum detection distance is thus expected to become shorter (longer). Therefore, numerical experiments with varying tsunami magnitude as well as the timing of the tsunami event based on long-term observation are necessary in future studies. In addition, methods of utilizing the statistically analyzed detection distance to mitigate tsunami impacts on coastal regions must be investigated.

The variance reduction was over 80% in ranges where the tsunami was detected, and less than 10% in ranges where the tsunami was not detected. Thus, we consider that the detected tsunami velocities can be quantitatively used to mitigate tsunami impact in addition to tsunami detection. This is a major concern, especially in Japan. In particular, it is crucial to estimate nearshore tsunami heights and check the category of tsunami warning issued by the JMA using measured tsunami heights or tsunami-induced

velocities in order to mitigate and understand tsunami impacts in coastal regions. For this reason, tsunami-induced velocities must be filtered out by using a high-pass filter. We used a 60-min moving average and showed the potential of the radar to adequately validate the warning category by a single case study. We believe that statistical analyses on the potential are needed, since the maximum detection distance and thus the accuracy of the velocity measurement at each range cell would vary depending on the sea surface state and tsunami magnitude.

In actuality, we cannot obtain the tsunami period in advance. The tsunami period becomes longer as M_w becomes greater. Considering that the wave period of the March 2011 tsunami was approximately 30–60 min, a high-pass filter with longer window size (i.e., 120 min) should be used in preparation for a longer wave period. When using the moving average to extract the tsunami-induced velocity component, BGCs over the time corresponding to the last half of the filter window cannot be obtained in real time; hence, the estimation of BGCs by using (for example) a linear extrapolation or autoregressive (AR) model (e.g., Fuji et al. 2015) will also be required. These methods should be carefully developed and examined since the estimation errors of longer-period components decrease the energy ratio, as mentioned in Subsection 2.3.1 . In this chapter,

we found that the exact extractions of BGCs are crucial to develop a real-time tsunami detection method.

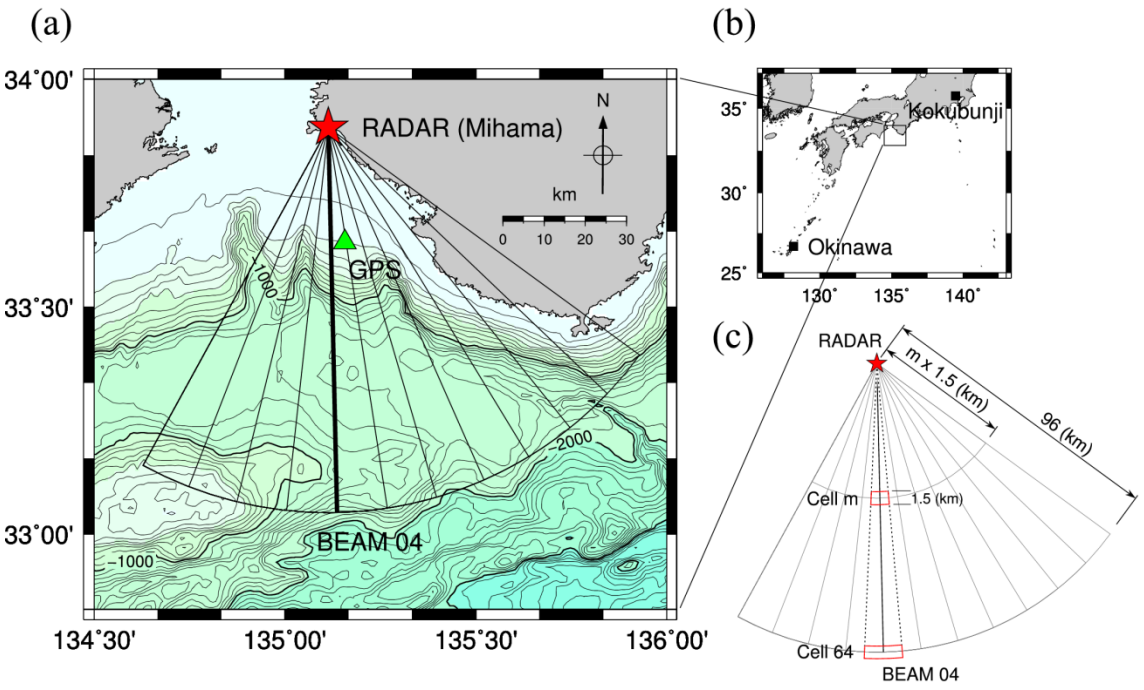

Fig. 2.1 a Observation area of the NJRC radar installed on the Mihama coast, Wakayama, Japan. The *red star* indicates the location of the radar and the *green triangle* indicates the location of the Wakayama-Nanseioki GPS wave gauge of NOWPHAS. **b** Location of ionosphere observation stations (Kokubunji, Okinawa) by NICT described in Subsection 2.3.4 . The distance between Kokubunji and Okinawa is 1471 km in grand circle distance. **c** Location of the range cell along beam 04 and the corresponding offshore distance from the radar

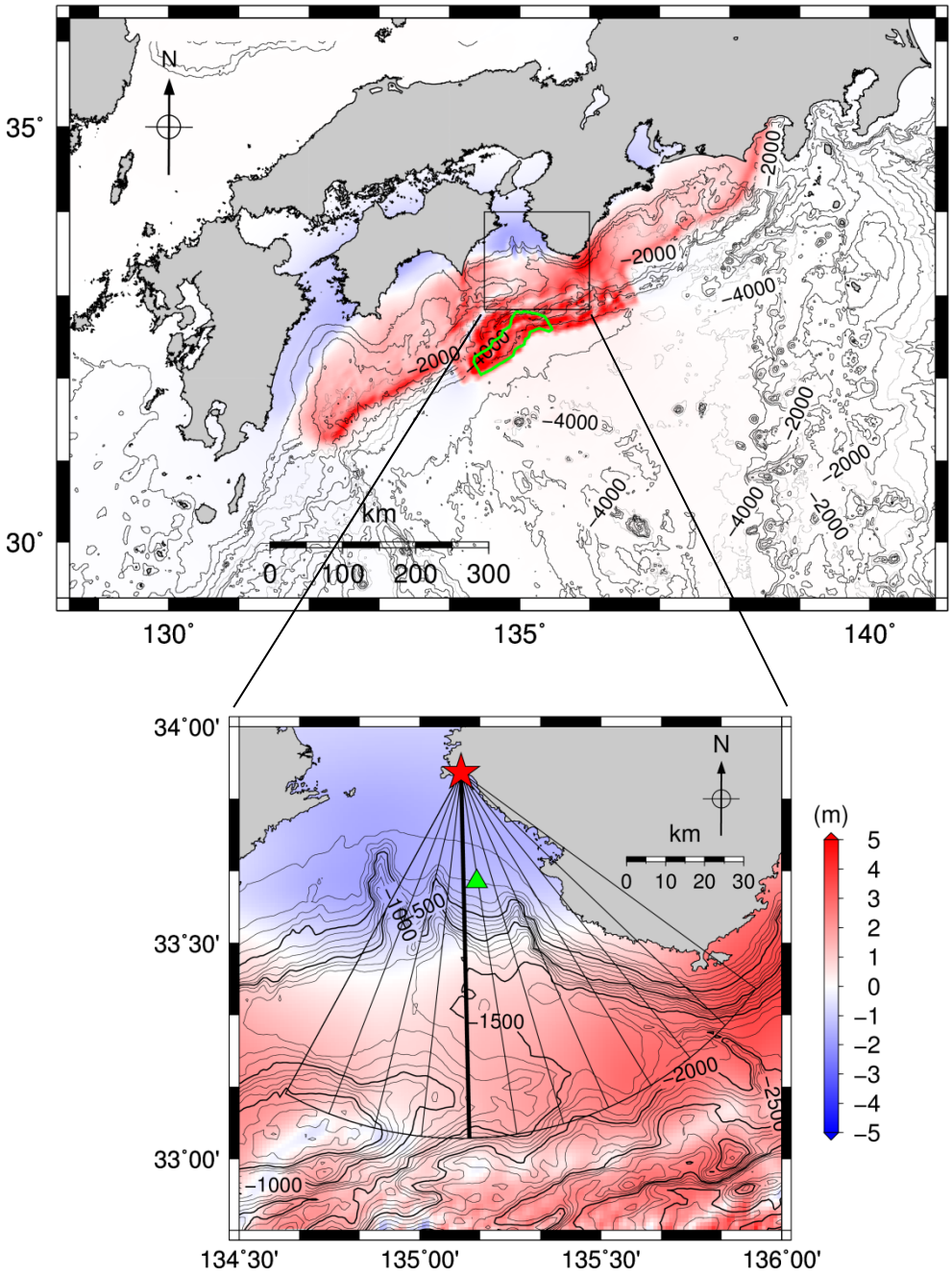

Fig. 2.2 Initial sea surface level caused by the Japan Cabinet Office's case 3 Nankai Trough earthquake. The area surrounded by a *green line* shows the area in which the slip is over 40 m

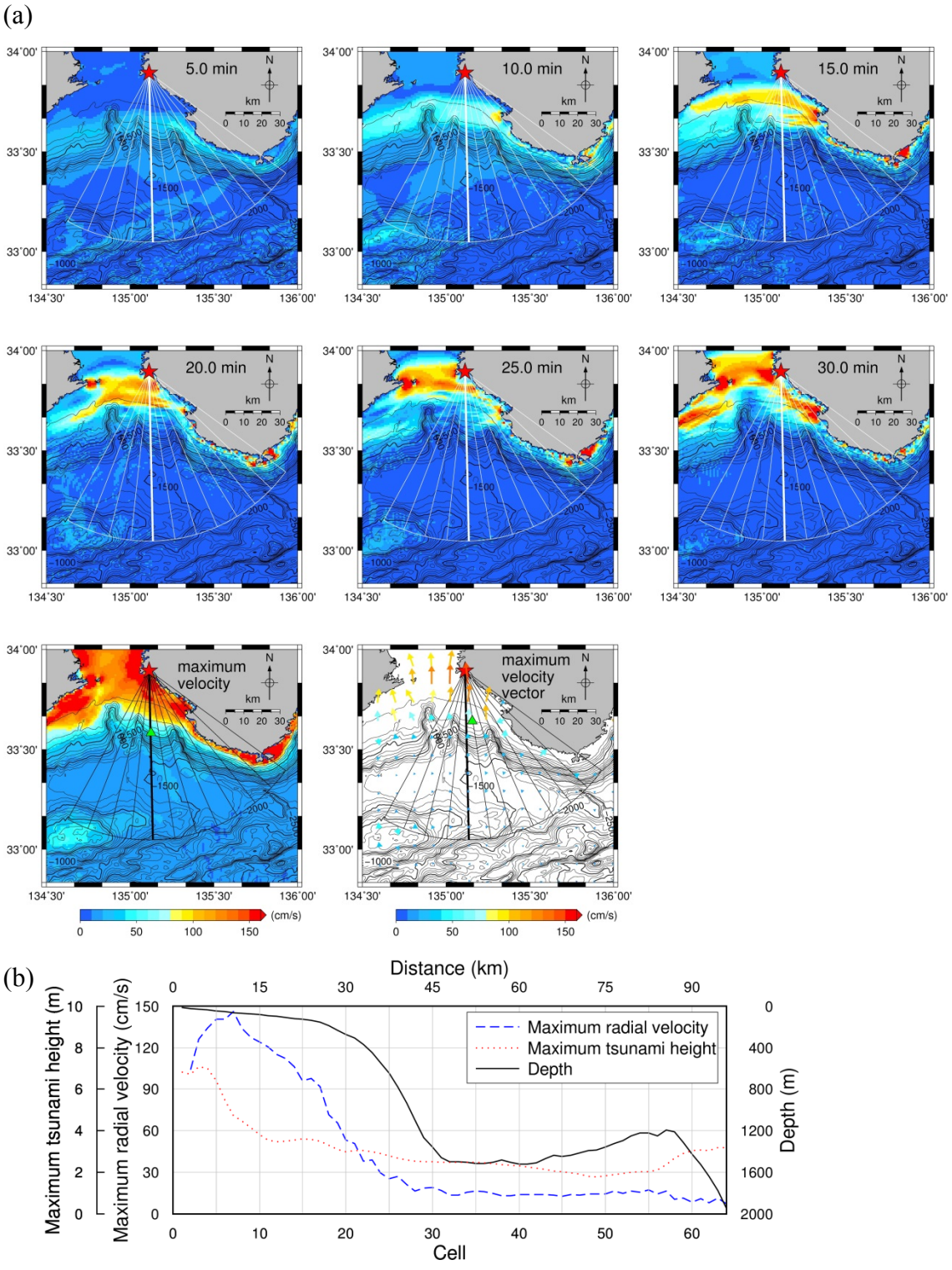

Fig. 2.3 a Temporal variations of tsunami velocities as the tsunami propagates (velocities at 5, 10, 15, 20, 25, and 30 min after the tsunami occurrence, the maximum velocity and the maximum velocity vector). **b** Dependence of the maximum radial velocity (*dashed blue*) and the maximum tsunami height (*dotted red*) on the water depth (*solid black*) upon the range cell on beam 04

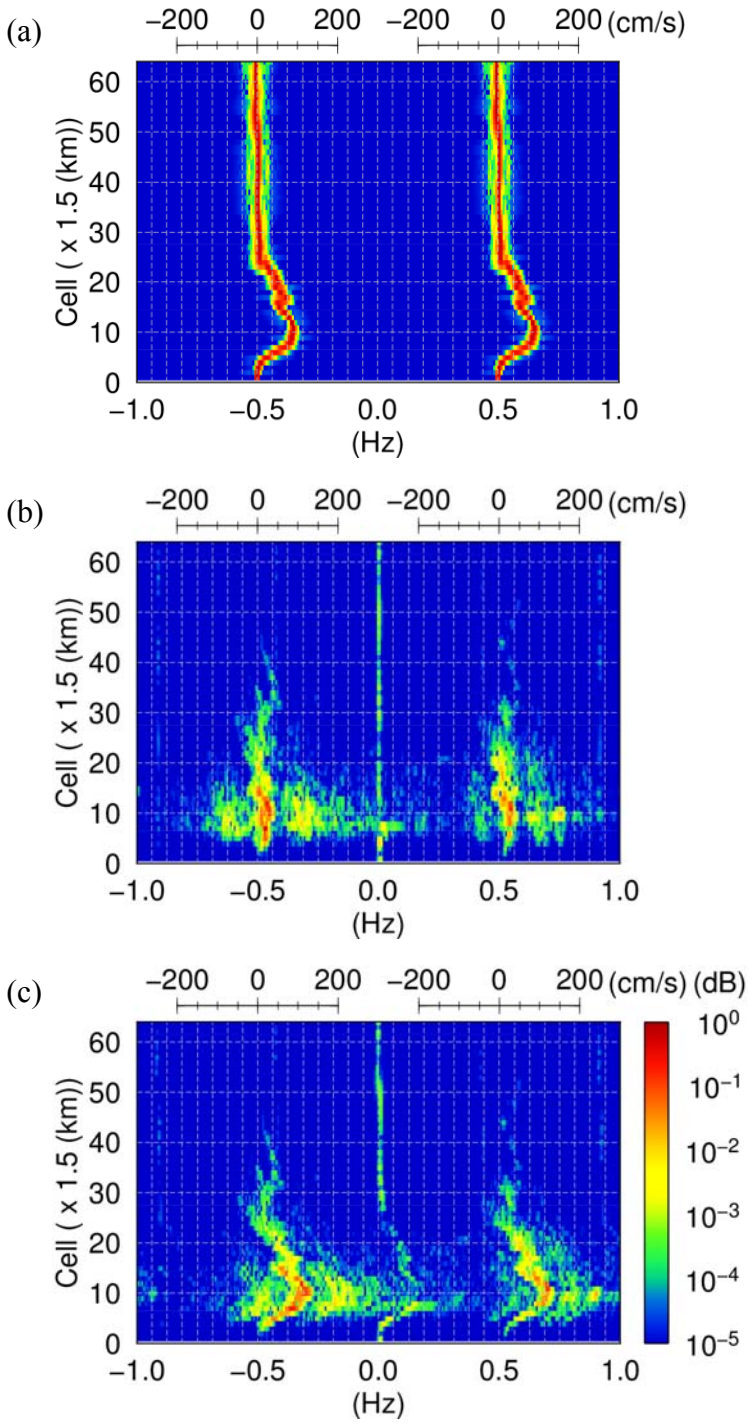

Fig. 2.4 a Doppler spectra of ideal signals (13 min after tsunami occurrence). **b** Doppler spectra of observed signals (06:13 on February 3, 2014). **c** Doppler spectra of synthetic signals, which would have been obtained 13 min after the event if the tsunami had been excited at 06:00 on February 3, 2014

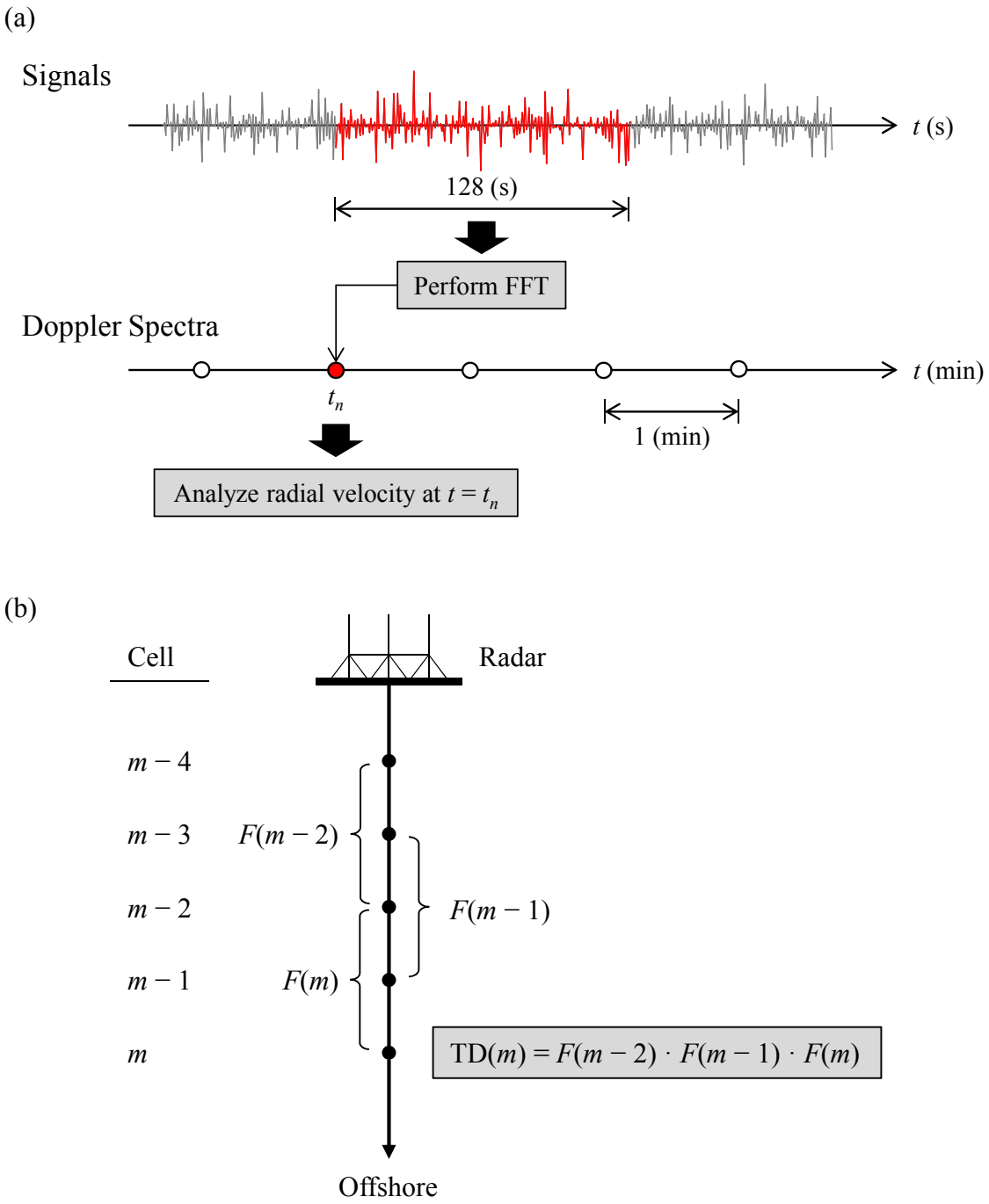

Fig. 2.5 Schematic illustration of a tsunami detection method in *a posteriori* analysis. **a** Relationship between location of signal periods (128 s) for calculating Doppler spectra and time of analyzed radial velocities. $v_{vt}(m, t_n)$, $v_{obs}(m, t_n)$, and $v_{sim}(m, t_n)$ were defined at $t = t_n$ (*red circle*). **b** Definition of a tsunami detection factor and corresponding significance functions

(a)

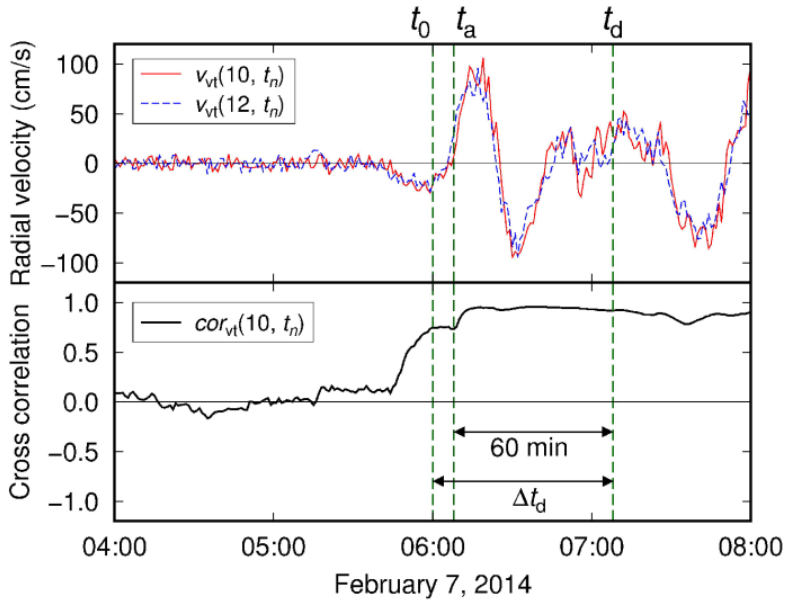

(b)

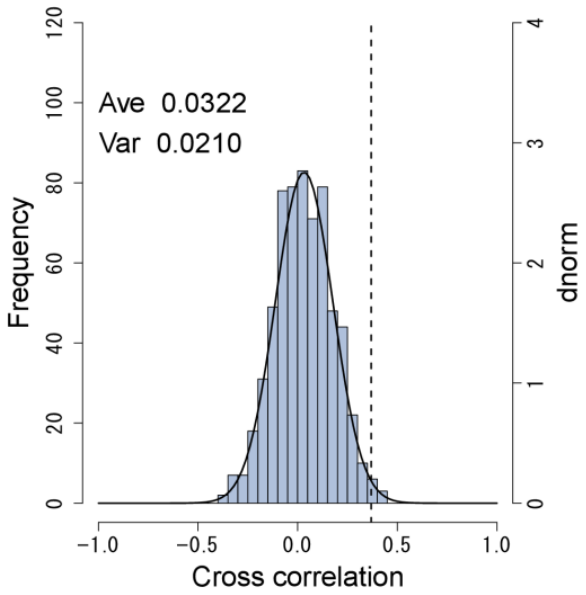

Fig. 2.6 a Temporal change in cross-correlation $\mathrm{cor}_{vt}(10, t_n)$ between $v_{vt}(10, t_n)$ (*solid red*) and $v_{vt}(12, t_n)$ (*dashed blue*) with the passage of tsunami assuming the tsunami was excited at 06:00 on February 7, 2014. t_0, t_a, and t_d indicate the time of tsunami occurrence, time of tsunami arrival, and 60 min after arrival, respectively. The emergence of negative velocities before $t = t_a$ is due to use of the 60-min moving average for extracting the shorter-period components from the synthesized velocities. **b** $P[\mathrm{cor}_{obs}(12, t_n)]$: Frequency distribution of the cross-correlation $\mathrm{cor}_{obs}(12, t_n)$ between $v_{obs}(10, t_n)$ and $v_{obs}(12, t_n)$. The dashed line indicates the value corresponding to the top 1% of $P[\mathrm{cor}_{obs}(12, t_n)]$

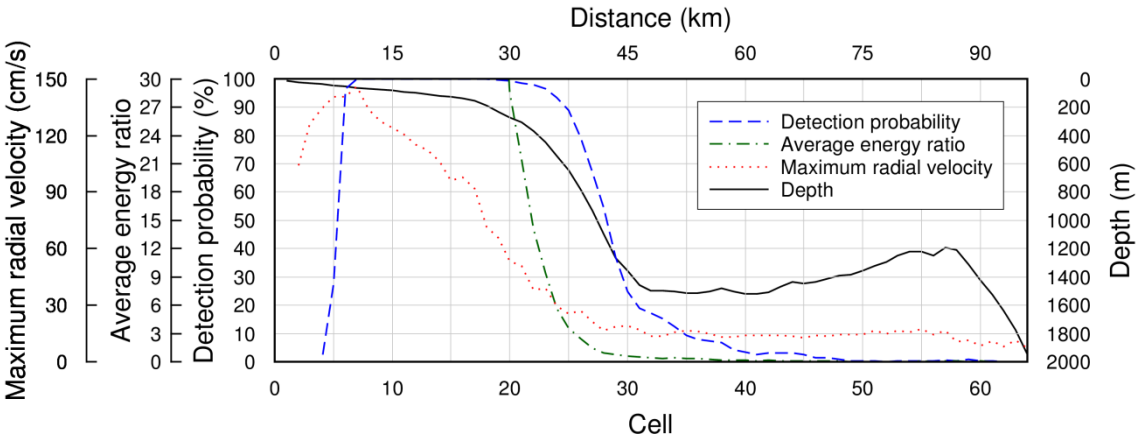

Fig. 2.7 Onshore-offshore distributions of the tsunami detection probability in February 2014 (*dashed blue*), the monthly average energy ratio (*dashed-dotted green*), the maximum tsunami-induced radial velocity (*dotted red*), and the water depth (*solid black*) along beam 04

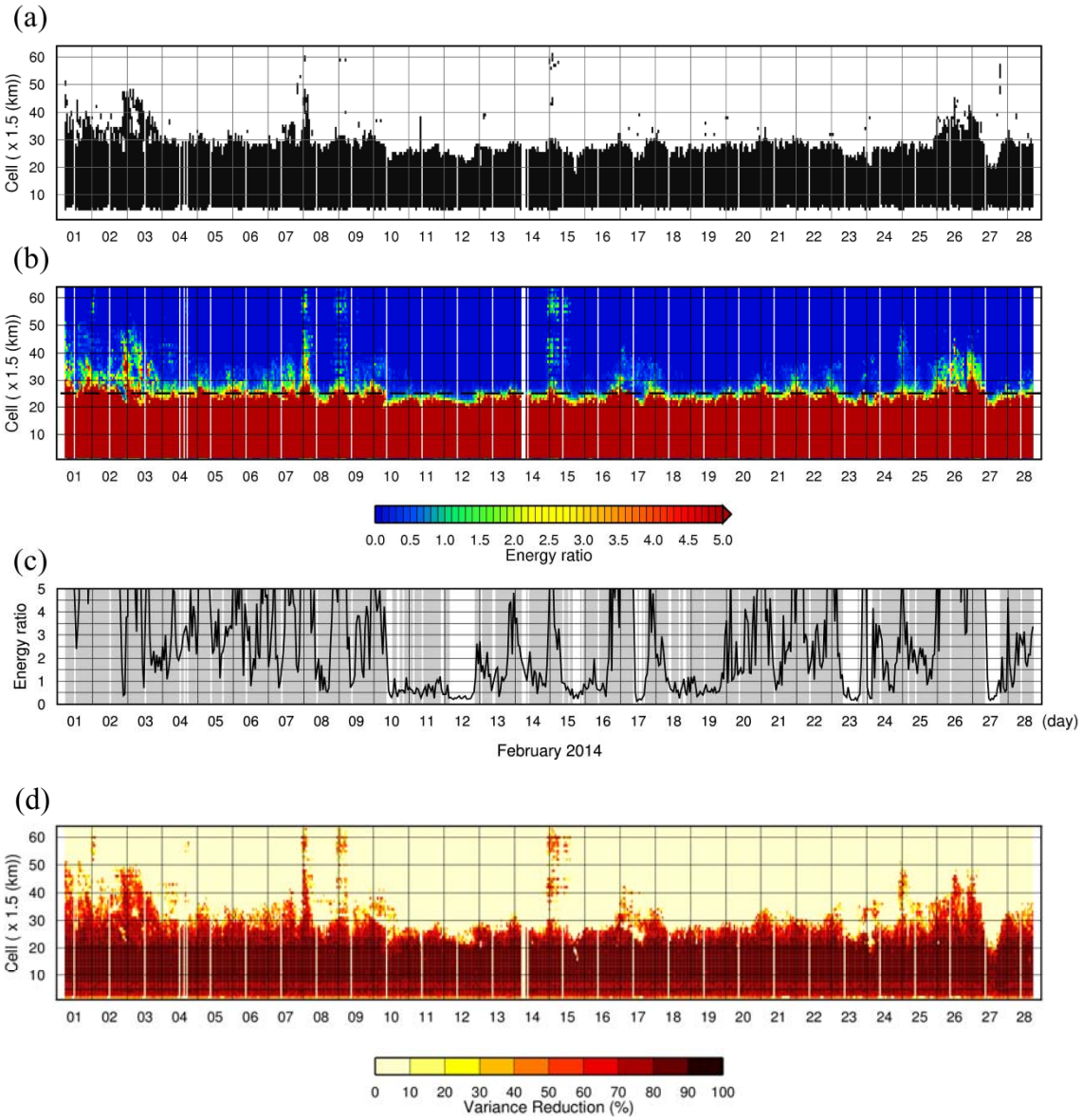

Fig. 2.8 a Time–distance diagram of the tsunami detection results along beam 04. The *black dot* indicates the cell where the tsunami was successfully detected (TD(m) = 1). **b** Time–distance diagram of the energy ratio between $v_{tsu}(m, t_n)$ and $v_{obs}(m, t_n)$. **c** Temporal variation of the energy ratio at cell 25. *Gray area* indicates the time and date when the tsunami was successfully detected. **d** Time–distance diagram of variance reduction

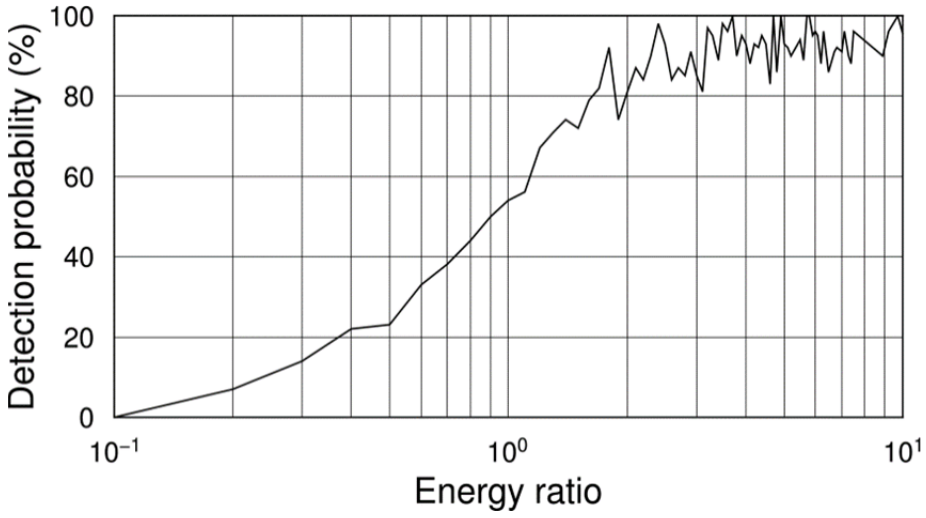

Fig. 2.9 Dependence of the detection probability on the energy ratio (0.1–10.0) divided in intervals by 0.1

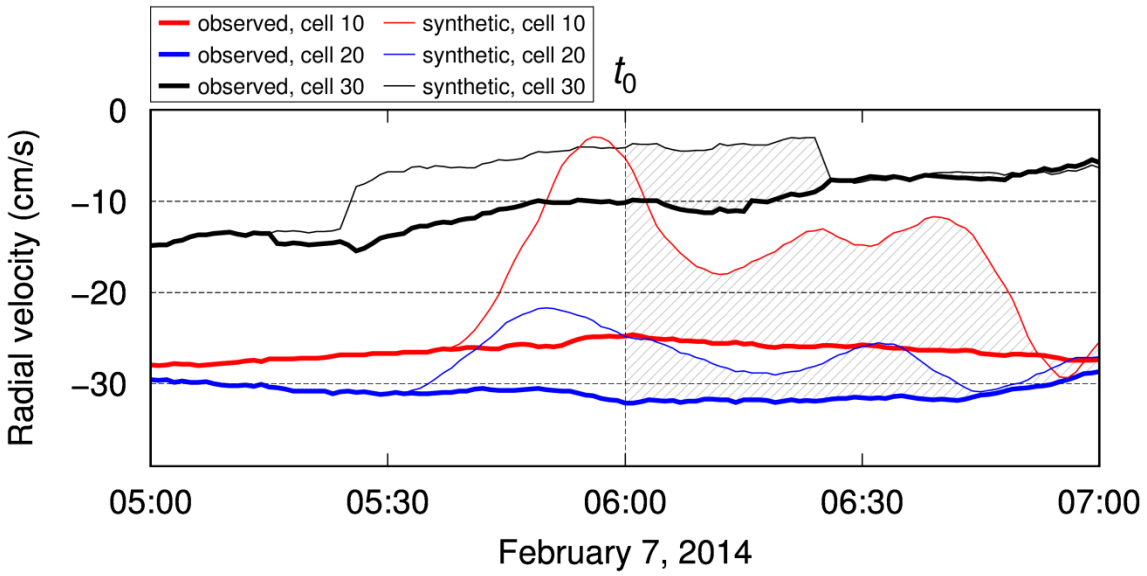

Fig. 2.10 Comparison of the longer-period components of synthetic velocities (*thin line*) and of observed velocities (*thick line*) at cells 10 (*red*), 20 (*blue*), and 30 (*black*) assuming the tsunami was excited at 06:00 on February 7, 2014. t_0 indicates the time of tsunami occurrence. The *hatched area* indicates the gaps of *thin line* and *thick line* from 06:00 to 07:00, which lead to underestimation of $v_{\mathrm{vt}}(m, t_n)$

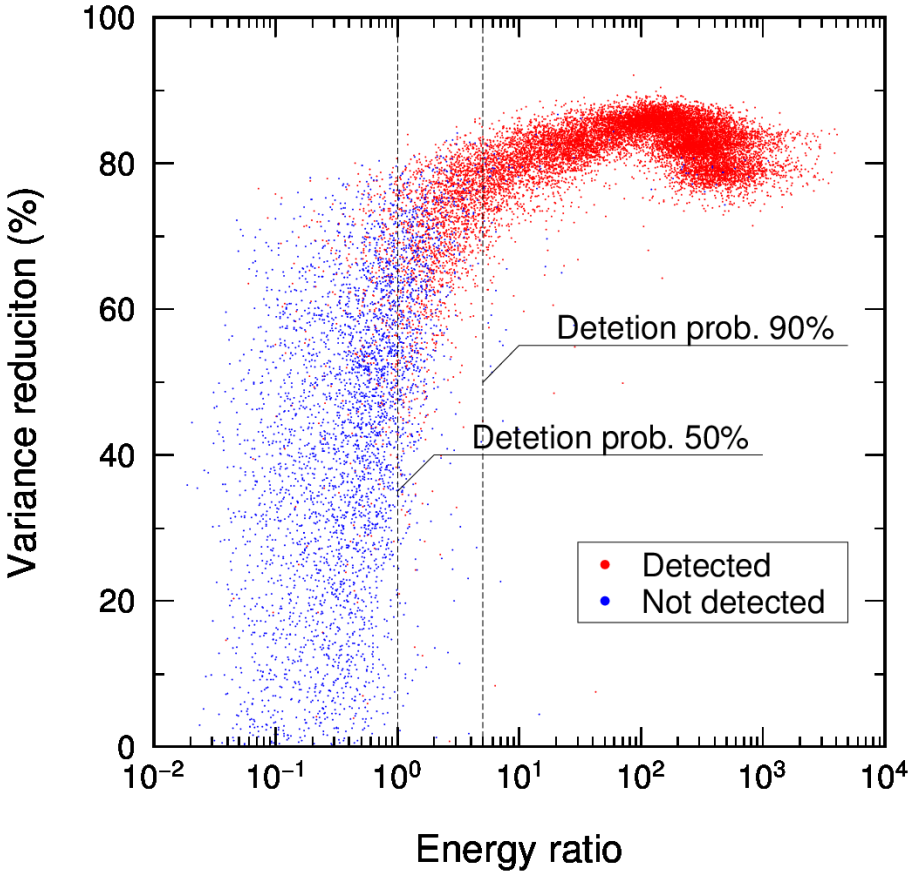

Fig. 2.11 Dependence of the energy ratio on the variance reduction

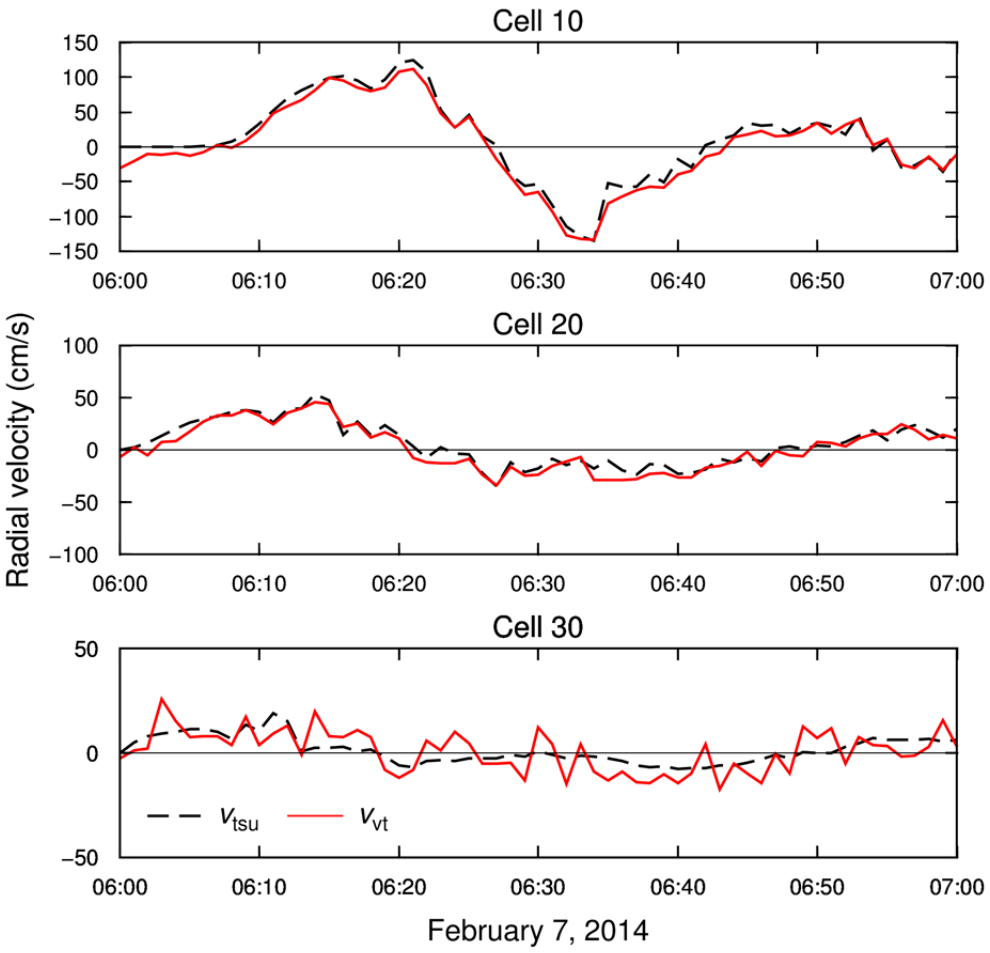

Fig. 2.12 Comparison of temporal variations of $v_{vt}(m, t_n)$ and $v_{tsu}(m, t_n)$ at cells 10, 20, and 30 assuming the tsunami was excited at 06:00 on February 7, 2014

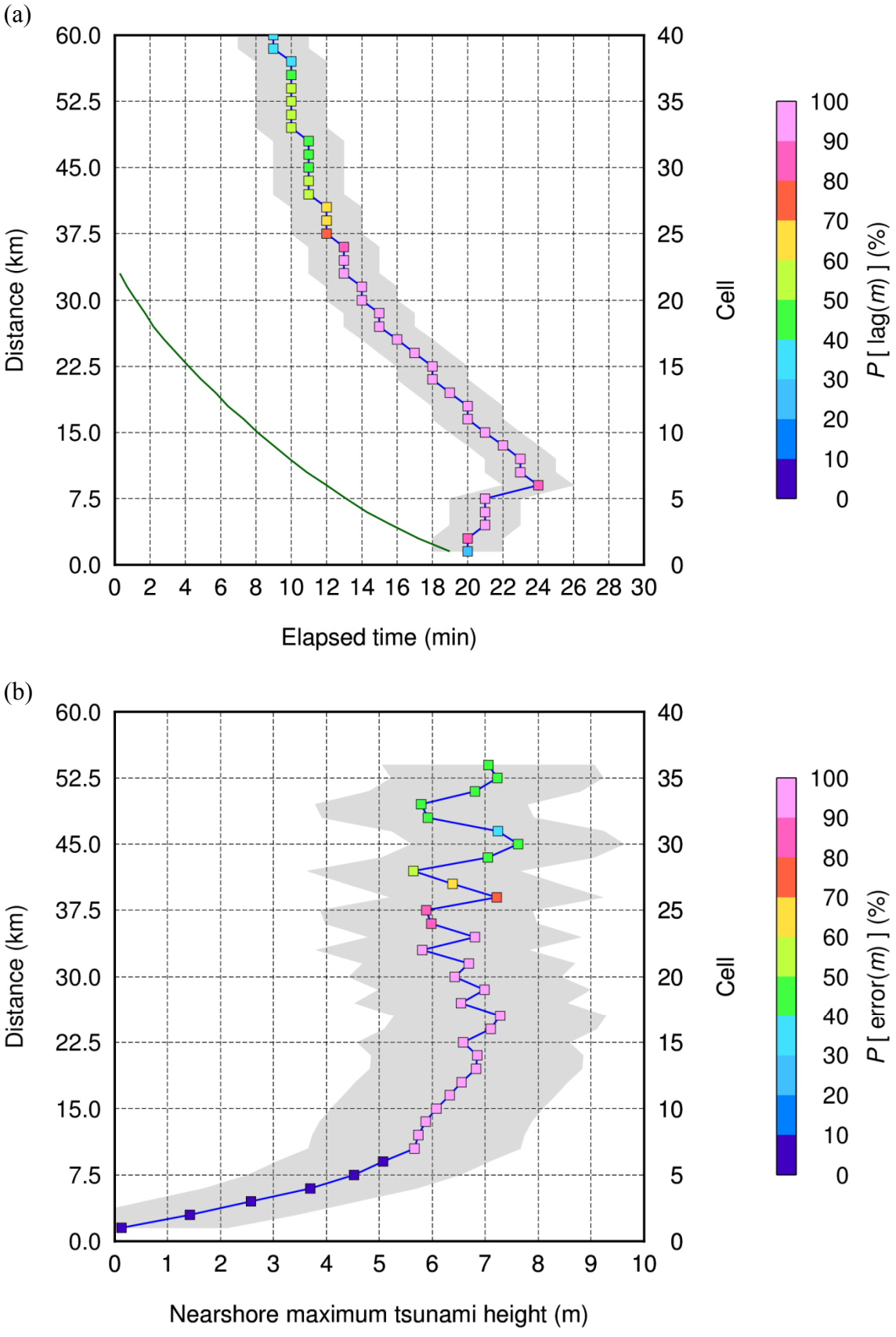
(a)
Distance (km)
Elapsed time (min)
Cell
P [lag(m)] (%)
(b)
Distance (km)
Nearshore maximum tsunami height (m)
Cell
P [error(m)] (%)

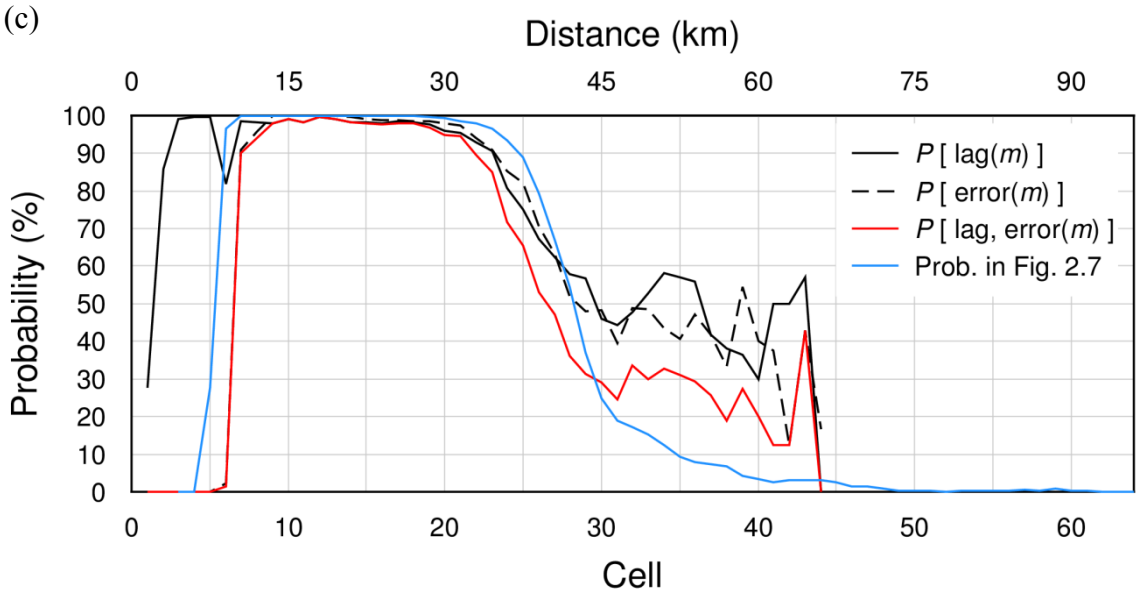

Fig. 2.13 **a** Time–distance diagram of tsunami propagation. The *green line* (theoretical tsunami wavefront) represents the theoretical curve back-calculating propagation from the speed of the linear long-wave starting from the time of tsunami arrival at the coast. The *blue line* represents the maximum velocities of the tsunami first wave. The *color scale* represents P[lag(m)] and light gray area means $|\text{lag}(m)| \leq 2$ min. **b** Variability of the maximum tsunami height near the coast estimated from offshore velocities along beam 04. The *color scale* represents P[error(m)] and the light gray area means $|\text{error}(m)| \leq 2$ m. The *blue line* represents tsunami height estimated from offshore velocity of numerical simulation. **c** Variability of P[lag(m)] (*solid black*), P[error(m)] (*dashed black*), and the joint probability of P[lag(m), error(m)] (*solid red*). The *light blue line* represents the tsunami detection probability in Fig. 2.7

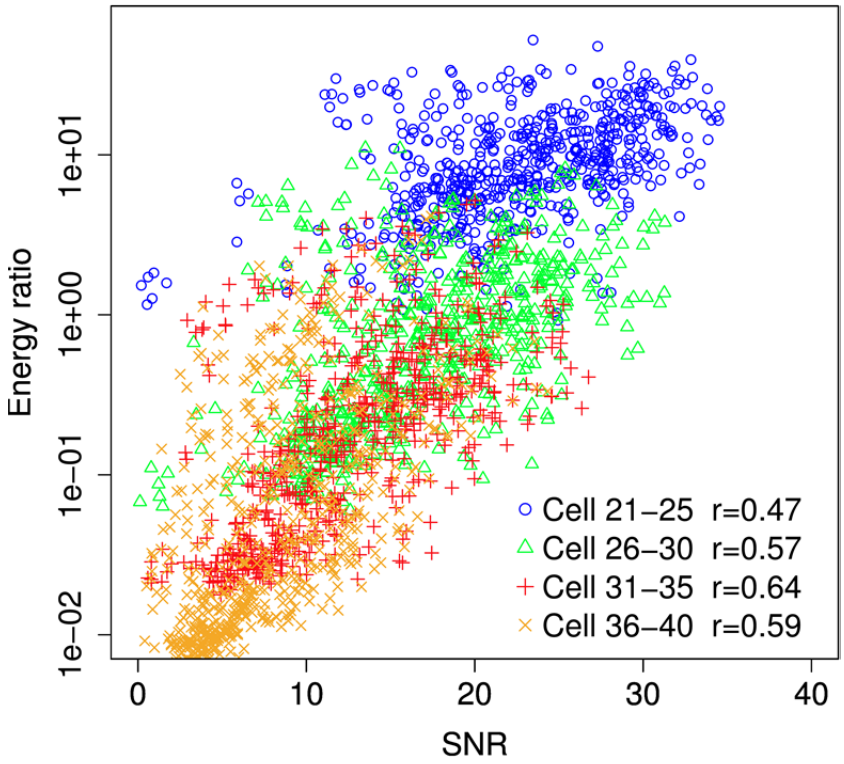

Fig. 2.14 Dependence of energy ratio over the continental shelf slope on five cell-averaged SNR values in cells 21–25, cells 26–30, cells 31–35, and cells 36–40

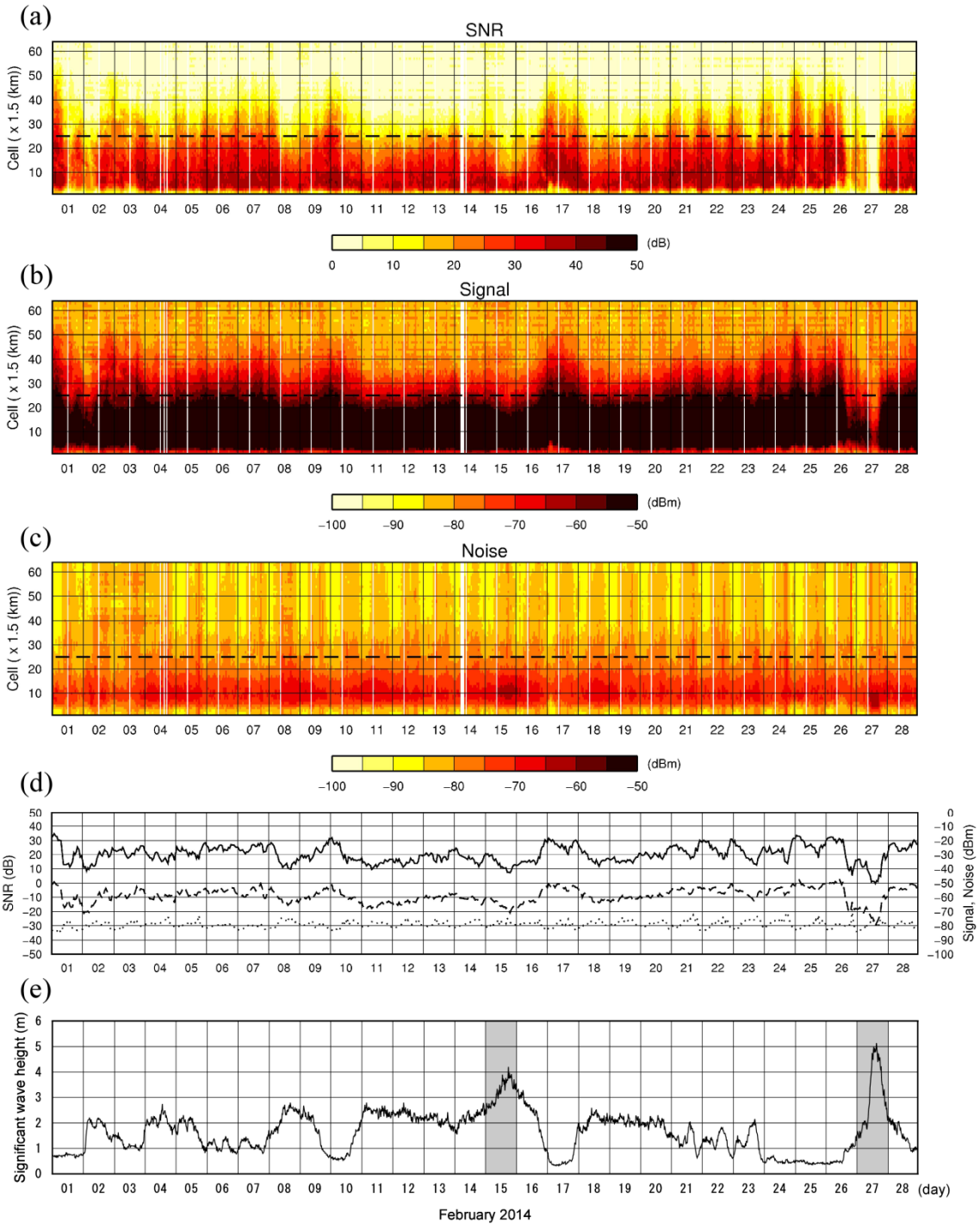

Fig. 2.15 a Time–distance diagram of SNR (60-min moving average). **b** Same as a, but for signal. **c** Same as a, but for noise. **d** Temporal variations of SNR (*solid*), Signal (*dashed*), Noise (*dotted*) at cell 25. **e** Temporal variation of significant wave heights observed by the Wakayama-Nanseioki GPS wave gauge. *Gray areas* indicate the date when extremely large wave heights were observed

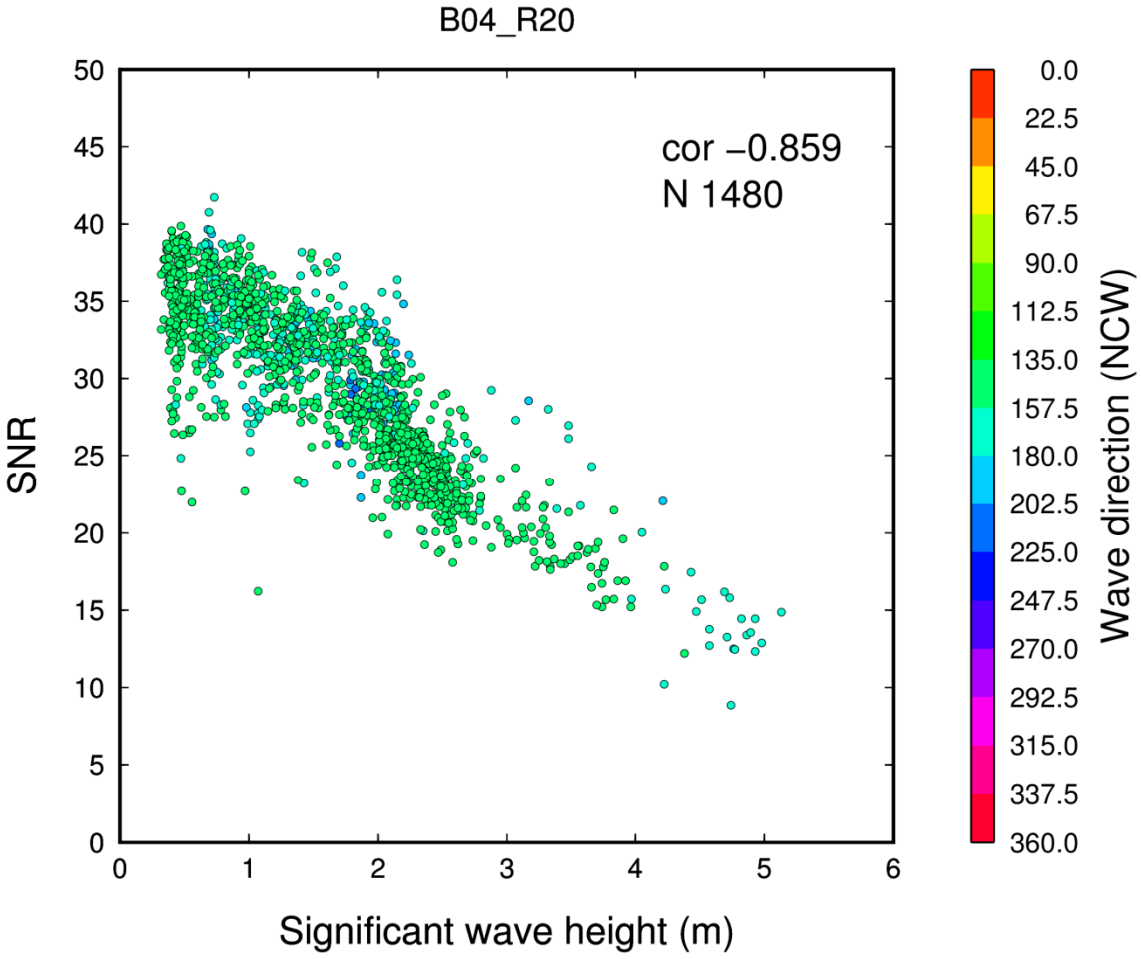

Fig. 2.16 Dependence of SNR at cell 20 along beam 04 on significant wave height observed by the Wakayama-Nanseioki GPS wave gauge (Fig. 2.1a). The plotted color indicates the wave direction measured clockwise from the north

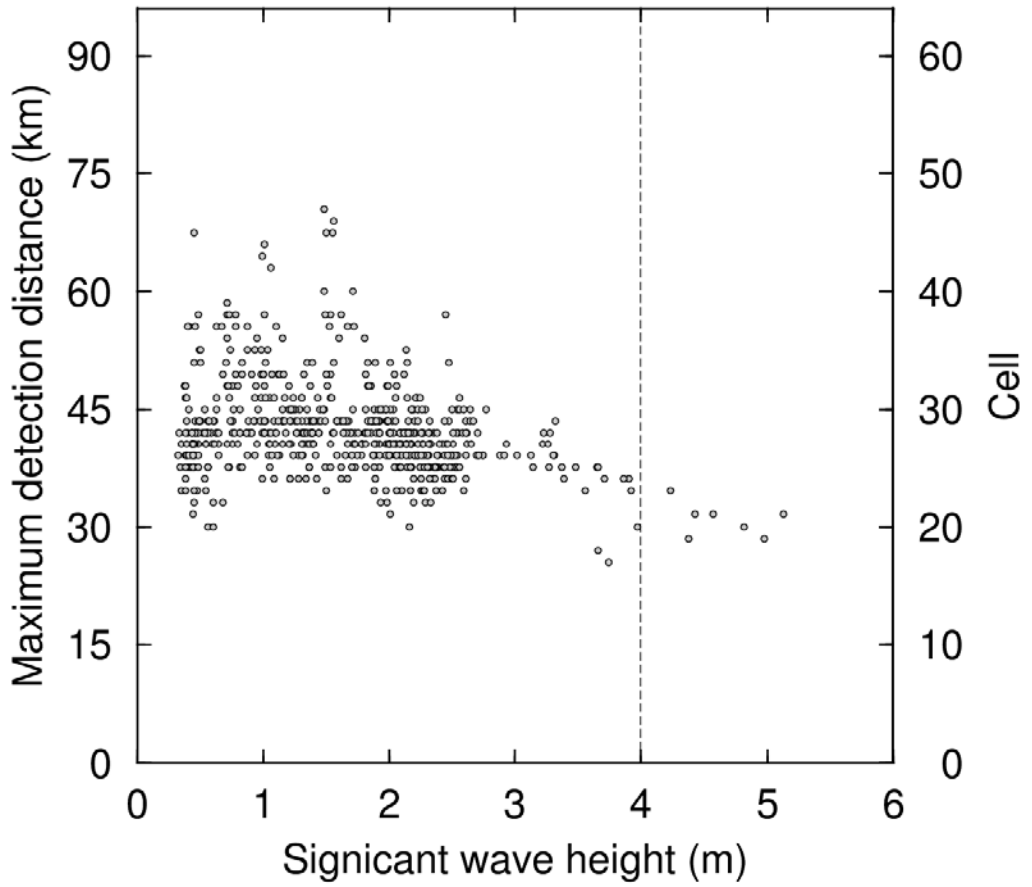

Fig. 2.17 Comparison of maximum detection distance on significant wave height observed by the Wakayama-Nanseioki GPS wave gauge (Fig. 2.1a)

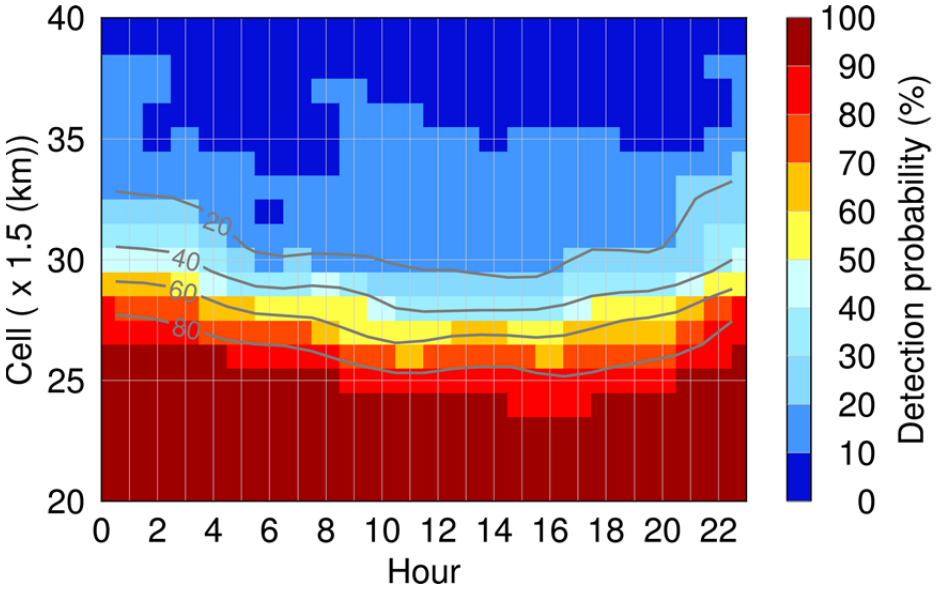

Fig. 2.18 Diurnal variation of the detection probability. Ensemble average is calculated except for February 15 and 27 when extremely large wave heights were observed. A 3-h moving average was then calculated

Table 2.1 System specifications of the NJRC (Nagano Japan Radio Co., Ltd.) HF radar

Radar type	FMICW (Frequency modulated interrupted continuous wave)
Center frequency	24.515 MHz
Sweep bandwidth	100 kHz (24.465–24.565 MHz)
Frequency sweep interval	0.5 s
Maximum transmission power	200 W (peak)
Range resolution	1.5 km
Velocity resolution	> 4.78 cm s^{-1}
Antenna type	One transmitting and eight receiving antennas (three-element Yagi)
Beamforming method	Multibeam DBF in broadside array
Beam width	12° (3 dB beam width)
Bearing resolution	±45° (in steps of 7.5°)

Table 2.2 Errors (Δv_{vt}) in calculation of total tsunami energy for 60 min caused by errors in extraction of longer-period components by using a 60-min moving average

Range cell number	Energy ratio	Detection probability (%)	Total energy for 60 min (cm^2/s^2) $\Sigma(v_{vt})^2$	$\Sigma(\Delta v_{vt})^2$	Increase (%)
10	317.4	100	2.0×10^5	7.0×10^3	3.5
20	28.6	100	2.8×10^4	9.8×10^2	3.5
30	0.6	25	6.1×10^3	1.1×10^3	17.5

Δv_{vt} corresponds to the hatched area in Fig. 2.10. The total energy of v_{vt} was calculated from the time series (red line) from 06:00 to 07:00 shown in Fig. 2.12

Table 2.3 Errors (Δv_{vt}) in calculation of total tsunami energy for 60 min caused by errors in extraction of longer-period components by using a 60-min moving average

				Estimation error				
Range cell number	Depth (m)	Simulated tsunami height (m)	Warning level	(offshore) Maximum velocity (cm/s)	(offshore) Maximum tsunami height (m)	Maximum tsunami height (m)	Maximum tsunami height (m)	Warning level
10	80	6.8	Major Tsunami	−12	−0.34	−0.58	5.19	Major Tsunami
20	270	6.8	Major Tsunami	−8	−0.42	−0.96	5.03	Major Tsunami
30	1,350	6.8	Major Tsunami	7	0.82	2.80	10.80	Major Tsunami

a Major Tsunami Warning: tsunami height is expected to exceed 3 m

Chapter 3

Evaluation of tsunami detection probability in real-time detection

3.1 Introduction

In Chapter 2, we examined the tsunami detection performance of the present method combined with the NJRC radar system through *a posteriori* analysis by setting the time of tsunami detection t_d as 60 min after tsunami arrival. However, to apply the tsunami detection method in practice, the tsunami arrival should be continuously judged in real time. Accordingly, it is important to evaluate the earliness of detection for practical tsunami disaster mitigation.

The first warning of the occurrence of a tsunami is issued by the JMA 3 min after an earthquake at present. However, the present JMA system still has a problem; the first warning may underestimate the true tsunami height especially for huge tsunamis as described in Section 1.2. This is crucial for tsunami disaster mitigation in Japan. We believe that real-time tsunami detection using HF radar is a key to continuously

checking the category of tsunami warning issued by the JMA in support of the present system.

Hence, in this chapter, we performed virtual tsunami observation experiments of February 2014 in real time by applying the present method and evaluated the tsunami detection probability and earliness of detection of a tsunami wavefront. Then, the results were compared with those by a previous method using q-factor proposed by Lipa et al. (2012a, b, 2014). Finally, application of the present method to tsunami disaster mitigation is discussed.

3.2 Materials and methods

3.2.1 Creation of virtually observed tsunami-induced velocities

In the *a posteriori* analysis in Chapter 2, we used 627 out of 660 synthetic signal event cases by eliminating 33 events due to intermittent system trouble. In this chapter, we additionally removed 37 events, which included missing data during 60 min before the time of tsunami detection in order to start to judge the tsunami wavefront immediately after tsunami occurrence. In total, 590 out of 660 events were analyzed: the timing of the tsunami event was the same as described in the *a posteriori* analysis,

which was set from 06:00 February 1, 2014 to 17:00 February 28, 2014 at 60-min intervals. In each case, the case 3 tsunami was used.

We used the same velocities of HF radar observation as the *a posteriori* analysis in Chapter 2: $v_{\mathrm{obs}}(m, t)$, which is the shorter-period component of the observed velocity, and which contains shorter-period BGC physics and BGN. In contrast, concerning virtually observed tsunami-induced velocities, we decomposed the shorter-period component $v_{\mathrm{vt}}(m, t)$ by using a 60-min moving average and an auto regressive (AR) model (e.g., Fuji et al. 2015) defined as Eq. (18) instead of using only a 60-min moving average in Chapter 2. We did this because, when using the moving average to extract the tsunami-induced velocities, BGCs over the time corresponding to the last half of the filter window size cannot be obtained in real time. Hence, we calculated the present BGCs by using a linear combination of past predictor value while shifting the time by 1 min:

$$x_t = \sum_{i=1}^{p} a_t x_{t-i} + \varepsilon_t \quad , \tag{18}$$

where x_t is the predictor, a_t is the parameter of the model (AR model coefficient), ε_t is the estimation error corresponding to white noise, the subscript t is time, and p is the

order of the AR model. $v_{vt}(m, t)$ is the synthesized radial velocity which additionally contains the tsunami-induced current.

3.2.2 Real-time tsunami detection method

The time of tsunami detection t_d was set from $t_0 - 60$ to $t_0 + 60$ min every 1 min. The tsunami detection methodology is almost the same as described in Chapter 2, but the definition of the cell at which tsunami arrival is judged is different. In real-time detection, we judge tsunami arrival at the time when the tsunami reaches cell $m - 2$ (the nearest cell of three adjacent range cells in Fig. 2.5b) in Eq. (8). Hence, we defined TDR(m), a tsunami detection factor for real-time detection, as follows (see also Fig. 3.1a):

$$\mathrm{TDR}(m) = F(m) \cdot F(m + 1) \cdot F(m + 2). \tag{19}$$

The value of TDR(m) at each cell was calculated for every 1 min from $t_0 - 60$ to $t_0 + 60$ min for 590 tsunami events. Tsunami detection was finally judged based on TDR(m): when TDR(m) = 1, we judged that the tsunami was detected at cell m.

Figure 3.1b shows the relationship between signal periods (128 s) for calculating Doppler spectra and the time of analyzed radial velocities in real-time analysis. Doppler

spectra are calculated by using 256-sample (128 s) FFT at $t = t_n$ based on discrete Fourier transform as follows:

$$F_k(m,t) = \sum_{l=0}^{N-1} X_l(m,t) \exp\left(-j\frac{2\pi}{N}kl\right), \tag{20}$$

where k and l are sequential numbers (k, $l = 0, \ldots, N-1$; $N = 256$), F_k is the Fourier coefficients and X_l is the synthetic signals. In the *a posteriori* analysis in Chapter 2, we let the time of X_0 be $t = t_n$, and then obtained F_k at $t = t_n$ by using future information of X_l (Fig. 2.5a). However, in real-time detection, we cannot use the future information of X_l. Hence, in this chapter, we let the time of X_{N-1} be $t = t_n$, and then calculated F_k at $t = t_n$ by using past information of X_l.

We considered factors affecting cross-correlation in real-time detection. Putting $\mathrm{cor}_{\mathrm{vt}}(m,t_n) = \mathrm{cor}'$, $v_{\mathrm{vt}}(m-2,t_k) = x_i$, $\overline{v_{\mathrm{vt}}(m-2)} = \bar{x}$, $v_{\mathrm{vt}}(m,t_k) = y_i$, and $\overline{v_{\mathrm{vt}}(m)} = \bar{y}$ in Eq. (7), and considering cross-correlation for 60 min, then $\mathrm{cor}_{\mathrm{vt}}(m,t_n)$ can be written as:

$$\mathrm{cor}' = \frac{\sum_{i=1}^{60}(x_i - \bar{x})(y_i - \bar{y})}{\sqrt{\sum_{i=1}^{60}(x_i - \bar{x})^2}\sqrt{\sum_{i=1}^{60}(y_i - \bar{y})^2}}. \tag{21}$$

Letting $S_{xx} = \sum {x_i}^2 - (\sum x_i)^2/60$, $S_{yy} = \sum {y_i}^2 - (\sum y_i)^2/60$, and $S_{xy} = \sum x_i y_i - \sum x_i \sum y_i/60$, then cor′ can be written as:

$$\mathrm{cor}' = \frac{S_{xy}}{\sqrt{S_{xx} S_{yy}}} \quad . \tag{22}$$

For example, if a tsunami is detected 3 min after arrival of the tsunami wavefront, the following assumption holds:

$$S_{xx} = \sum {x_i}^2 - \frac{(\sum x_i)^2}{60} \approx \sum {x_i}^2 \quad , \tag{23}$$

$$S_{yy} = \sum {y_i}^2 - \frac{(\sum y_i)^2}{60} \approx \sum {y_i}^2 \quad . \tag{24}$$

Taking into account that x and y are almost uncorrelated before the arrival,

$$\begin{aligned} S_{xy} &= \sum x_i y_i - \frac{\sum x_i \sum y_i}{60} \\ &\approx x_{58} y_{58} + x_{59} y_{59} + x_{60} y_{60} - \frac{(x_{58} + x_{59} + x_{60})(y_{58} + y_{59} + y_{60})}{60} \quad . \end{aligned} \tag{25}$$

Assuming the velocity scale of x and y after the arrival is almost the same, S_{xy} can be approximated by:

$$S_{xy} \approx {x_{58}}^2 + {x_{59}}^2 + {x_{60}}^2 - \frac{(x_{58} + x_{59} + x_{60})^2}{60} \approx {x_{58}}^2 + {x_{59}}^2 + {x_{60}}^2 \quad . \tag{26}$$

Finally, we obtain the following relation:

$$\mathrm{cor}' \approx \frac{\sum_{i=58}^{60} (x_i)^2}{\sum_{i=1}^{60} (x_i)^2} = \frac{1}{\frac{1}{E'_{\mathrm{ratio}}} + 1} \quad , \tag{27}$$

where

$$E'_{\text{ratio}} = \frac{\sum_{i=58}^{60} (x_i)^2}{\sum_{i=1}^{57} (x_i)^2} \quad (28)$$

E'_{ratio} represents the kinetic energy ratio before and after arrival of the tsunami wavefront: namely, the ratio of the shorter-period components between tsunami-induced currents and BGCs including BGN. Clearly, the expressions of cross-correlation Eq. (27) and energy ratio Eq. (28) are quite similar to Eqs. (13) and (14) in the *a posteriori* analysis. After all, this indicates that the probability of detecting the tsunami wavefront primarily depends on the energy ratio of tsunami-induced current and BGC.

3.3 Results and discussion

3.3.1 Real-time detection distance and earliness of tsunami detection

Figure 3.2 shows a time-–distance diagram of detection result assuming the tsunami was excited at 06:00 on February 1, 2014. The red circle represents the location and the time when the tsunami was detected. The background color contour represents $v_{\text{vt}}(m, t_n)$. The green line represents the theoretical curve obtained by back-calculating propagation from the speed of the linear long-wave starting from the time of tsunami

arrival at the coast. Again, the tsunami arrival time at the coast was defined as the time when the radial velocity calculated by the numerical tsunami model $v_{tsu}(1, t)$ first exceeds ± 4.78 cm/s, which is identical to the velocity resolution of the radar. This line means the time of manifestation of tsunami-induced velocity (theoretical tsunami wavefront) in each cell. From Fig. 3.2, it is clear that the tsunami was continuously detected after $v_{vt}(m, t_n)$ started to increase with time. We made the time–distance diagram for 590 events in the same way.

Figure 3.3, representing radial velocities of $v_{vt}(m, t_n)$ obtained by using a 60-min moving average and AR model along beam 04 after the occurrence of the tsunami, showed that two peaks of the first and the second wave were clearly detected (e.g., cells 11 and 17 at "Elapsed time = 15 (min)"). The waveform and the peak velocities of $v_{vt}(m, t_n)$ are in good agreement with those of $v_{tsu}(m, t_n)$. These are of great importance for tsunami disaster mitigation, because the maximum peak velocity of the wave leads to the maximum wave height on the coast, causing great damage.

We evaluated the earliness of tsunami wavefront detection, which is a key for tsunami disaster mitigation. Figure 3.4 shows the frequency distribution of the detection result of February 2014. The height of the scale bar represents the sum of the earliest detected events in each cell. The color represents the average energy ratio. The green

line is the theoretical tsunami wavefront. No misdetection was found before the time of manifestation of the theoretical tsunami wavefront.

Focusing on the maximum value of the detected events, the tsunami was detected within approximately 3 min after the time of manifestation in ranges from cell 2 to 14. The time lag between manifestation and detection increased beyond cell 15, which is the location of the continental shelf edge. This suggests that in offshore ranges beyond the shelf edge where the tsunami-induced velocity is rather small (Fig. 2.3a), a longer time is required to accumulate the tsunami energy in order to raise the energy ratio sufficiently to detect the tsunami arrival.

3.3.2 Difference of detection distance between real-time and *a posteriori* analysis

Figure 3.5 shows the time–distance diagram of the maximum detection distance comparing real-time analysis and *a posteriori* analysis for the 590 tsunami events. The red line represents the distance by real-time analysis. The furthest cell for the earliest detection time (blue circle in Fig. 3.2) in each event was plotted. The blue line represents the distance, which is the consecutive detection distance from the radar location, obtained by *a posteriori* analysis. In general, the distance obtained by real-time analysis was shorter than that by *a posteriori* analysis. From a comparison of the

distances in Fig. 3.6, the average of the difference was estimated to be approximately 10 km (L = 29 km in real-time and L = 39 km in *a posteriori*).

Figure 3.7 shows a comparison of the energy ratio between real-time analysis and *a posteriori* analysis. The average energy ratio of the two were $O(10^0)$ and $O(10^1)$, respectively. Clearly, the average by *a posteriori* analysis is one order of magnitude greater than that by real-time analysis. This is because the tsunami energy can be sufficiently accumulated in the *a posteriori* analysis since the time of detection is set to 60 min after tsunami arrival, whereas the tsunami energy is barely accumulated in the real-time analysis since the tsunami arrival was detected in a few minutes after manifestation of the theoretical wavefront. This result demonstrates the relations of Eqs. (27) and (28).

Figure 3.8a shows the time–distance contour plot of tsunami detection probability of February 2014. The pink line represents the theoretical tsunami wavefront. The maximum detection distance with 80% detection probability and 4-min time lag was cell 15 (L = 22.5 km). The detection probability in a range direction beyond cell 20 significantly dropped to around 10% at cell 25. From Fig. 3.8b, in ranges from cell 1 to 15, the detection probability rapidly increased to 80% within 4 min after the time of manifestation of the theoretical tsunami wavefront, then reached around 100%. In

contrast, in offshore ranges beyond cell 15, the speed of the increase gradually became moderate and the probability did not reach 100%.

Here, we examine the energy ratio required for the detection by comparing that in the real-time analysis and *a posteriori* analysis. Figure 3.9 shows the contour plot of average energy ratio. From the comparison between Fig. 3.8a and Fig. 3.9, the energy ratios with 80% detection probability at cells 9 and 15 (corresponding time is 12 and 8 min) are estimated to be 1, and those with 50% detection probability at cells 8 and 14 (corresponding time is 12 and 8 min) are estimated to be 0.5. Meanwhile, Fig. 2.7 indicates that the energy ratio corresponding to 80% (50%) detection probability is 3 (1). Thus, the order of the energy ratio necessary for detection was distinctly different: $O(10^{-1})$ for real-time analysis and $O(10^{0})$ for *a posteriori* analysis.

The reason for the difference can be understood as follows. Focusing on the time 60 min after manifestation of the theoretical tsunami wavefront, Fig. 3.9 suggests that the ranges in which the corresponding energy ratio is $O(10^{-1})$ are located far offshore beyond the continental shelf edge (cell 20). Moreover, Fig. 3.10 indicates that cross-correlation increased very slowly with time and did not increase readily in these ranges. This is because larger BGN in offshore ranges prevents a rapid increase of the cross-correlation. The BGN rapidly increased beyond the shelf edge in the experiment.

After all, in the *a posteriori* analysis, tsunami detection was not possible far offshore beyond the shelf edge. Therefore, the order of the energy ratio necessary for detection in the *a posteriori* analysis becomes one order of magnitude greater than that in the real-time analysis since the tsunami energy is sufficiently accumulated for 60 min after manifestation of the theoretical wavefront.

3.3.3 Comparison of real-time detection probability with previous method

Lipa et al. (2012a, b, 2014) proposed a tsunami arrival detection algorithm using the CODAR SeaSonde® system based on pattern recognition, which uses the temporal change of cross-correlation, which is over the past two adjacent time intervals of the spatially averaged velocities within 2–6-km wide bands parallel to the coast. They defined the tsunami arrival when a factor (which they called q-factor) representing the change of the cross-correlation exceeds a preset threshold. The threshold is empirical and they set the value to ±500 for the Nankai Trough earthquake. The q-factor is calculated as follows:

(i) Calculate velocities in the direction perpendicular to the depth contours from radial velocities in area bands 2-km wide and approximately parallel to the depth contours.

(ii) Average these velocities over the bands in order to decrease noise included in the observed signal.

(iii) Define a velocity deviation function $D(t)$ at time t, which consists of the product of the velocity deviation from background over three adjacent bands.

(iv) Define a velocity increment function $\Delta V(t)$ at time t, which consists of the sum of the velocity change from $t - 2\delta$ to t over the bands, where δ is time interval.

(v) Calculate a correlation function $C(t)$, which is set to 100 when the velocity increases or decreases with time for all three area bands from $t - 2\delta$ to $t - \delta$, and $t - \delta$ to t, otherwise set to 1.

(vi) Define q-factor at time t, which consists of the velocity deviation function $D(t)$, the velocity increment function $\Delta V(t)$, and the correlation function $C(t)$:

$$q(t) = C(t) \cdot \Delta V(t) \cdot D(t). \tag{29}$$

We examined detection probability by applying their method using q-factor to the virtual tsunami observation experiments of February 2014 along beam 04. Figure 3.11a shows the time–distance plot of detection result. The result was plotted at the nearest cell of the three adjacent cells. It was found that the tsunami wavefront was detected within 1–2 min after the time of manifestation of the theoretical tsunami wavefront in

ranges from cell 2 to 17 with more than 80% probability. Meanwhile, misdetections frequently occurred with around 10% probability (light pink circle in Fig. 3.11a). Figure 3.11b shows the histogram of q-factor calculated from $v_{obs}(m, t_n)$ at cell 9 to 11, 19 to 21, and 29 to 30. The q-value exceeds ±500 even when a tsunami does not occur. This leads to many false alarms in real-time detection. The magnitude of observed velocity in their study was around 15 cm/s and that of this study in the Kii Channel was around 150 cm/s. This suggests that the threshold should be much greater than ±500 in the Kii Channel to avoid misdetection.

Figure 3.12a shows detection probability by using q-factor with the threshold set to ±100,000 (200 times greater compared with the preset value). The misdetections completely disappeared but detection probability decreased. In detail, the detected time of the tsunami wavefront was delayed by about 1 min and the maximum detection distance was shortened by around 5 cells (L = 7.5 km) (Fig. 3.11a, Fig. 3.12a).

Figure 3.12b shows detection probability based on the method proposed in this study using cross-correlation. No misdetection was found and detection probability at the time of tsunami arrival was almost the same as that by q-factor with the threshold of ±500 in ranges from cell 2 to 15. Tsunami arrival was detected within 3–5 min (2–3 min delay compared with the time detected by q-factor) after the time of manifestation of

tsunami-induced velocity. The delay is caused by the difference of the time interval used for calculating cross-correlation. The q-value by their method was calculated over two adjacent time intervals (i.e., past 2 min in this study). In contrast, the cross-correlation in the present method was calculated by using $v_{vt}(m, t_n)$ obtained for 60 min. We believe that the delay could be resolved by using a shorter period such as 30 min to calculate the cross-correlation.

Moreover, it is clear that the method using q-factor detected the subsequent second tsunami wavefront in addition to the first wavefront (Fig. 3.12a). Meanwhile, the present method using cross-correlation continuously detected tsunami wavetrains after detecting the first wavefront.

3.3.4 Applicability of tsunami detection methods

Tsunami detection by using HF radar should be assessed based on a combination of radar system specifications and detection method. As we described in the previous subsection, according to Lipa et al. (2012a, b, 2014), the CODAR SeaSonde® system uses averaged velocities over bands parallel to the coast in order to reduce BGN, supposing that the depth contours are approximately parallel to the coast. This indicates that it is difficult to use the measured average velocities, for example, to check the

category of tsunami warning issued by the JMA, since the velocities are spatially averaged along the coast and will be rather small compared to the actual tsunami-induced velocities. In particular, it is almost impossible to check the category for complex bathymetries where the depth contours are not parallel to the coast such as the southern coast of Honshu Island. In contrast, as we demonstrated in Subsection 2.3.2 , we can check the category by the NJRC radar-derived velocities without spatial averaging, which means the NJRC radar system can be used to check the category for complex bathymetries. These NJRC radar-derived velocities could also be used to estimate the tsunami source (e.g., initial sea surface level) by using inversion methods (Satake 1987; Tsushima et al. 2009, 2011, 2012; Fuji et al. 2013), which would enable us to specify areas at risk of devastating damage by numerical simulations using the estimated initial sea surface height as an initial condition.

Concerning tsunami detection, here we have shown two methods (q-factor and cross-correlation method). For q-factor, $D(t)$ represents the ratio between tsunami-induced velocity and BGC velocity; $\Delta V(t)$ represents the velocity change due to arrival of the tsunami wavefront; $C(t)$ is a correlation function and the value is empirically decided. The value of $q(t)$ is calculated by taking the product of the three functions of Eq. 29 and hence the physical meaning of the value, which consists of the

three functions, is not clear in terms of tsunami physics. In contrast, the cross-correlation method has a physical meaning since it primarily depends on the energy ratio between tsunami current and BGCs. Therefore, it would be possible to roughly estimate tsunami detection probability in other coastal regions without conducting virtual tsunami observation experiments (Subsection 2.3.1). In addition, the cross-correlation method can detect not only tsunami wavefront but also subsequent wavetrains (Fig. 3.12b), which is useful for cancelling an issued tsunami warning at the right time.

q(t) is more sensitive in detecting a tsunami wavefront (Fig. 3.11a, Fig. 3.12a) than the cross-correlation method, because it is calculated from the velocities obtained from $t - 2\delta$ to t, which is 2 min for our case using the NJRC radar system. However, Eqs. (27) and (28) demonstrate that calculating cross-correlation at shorter time intervals increases the sensitivity of tsunami wavefront detection for the cross-correlation method. We will examine the sensitivity of wavefront detection using shorter time intervals such as 30 min in the near future.

When using q-factor or the cross-correlation method combined with the CODAR SeaSonde® system, we need to conduct spatial averaging of measured velocities prior to the tsunami detection. Thus, we cannot detect spatial extension of the wavefront. In

contrast, we would be able to detect the wavetrain by using the cross-correlation method with the CODAR SeaSonde® system in regions with simple bathymetries where the depth contours are parallel to the coast. When we use q-factor or the cross-correlation method combined with the NJRC radar system, we can detect the spatial extension of the wavefront, and also detect the wavetrain by using the cross-correlation method even for regions with complex bathymetries.

To summarize, the combination of the NJRC radar system with the cross-correlation method was found to be efficient for tsunami disaster mitigation for complex bathymetries in Japanese coastal regions in terms of detecting the first tsunami wavefront and subsequent wavetrains, with no misdetection. Tsunami detection probability by using this combination depends on the tsunami magnitude and local bathymetry. Hence, the detection probability should be carefully examined under various tsunami scenarios and bathymetries for various combinations of detection method and radar system.

3.4 Summary

We statistically examined the real-time tsunami detection probability of February 2014 by applying the virtual tsunami observation experiments developed in Chapter 2.

Virtually observed tsunami velocities were created by using the moving average and AR model in order to estimate the shorter-period components of BGC in real time.

In the experiments, the maximum detection distance with 80% detection probability and 4-min time lag was cell 15 (L = 22.5 km). Tsunami arrival was detected within approximately 3 min after the time of manifestation of tsunami-induced velocity in ranges from cell 2 to 14. However, the time lag started to increase beyond cell 15. This suggests that in offshore ranges where the tsunami-induced velocity is rather small, it takes much longer to accumulate the tsunami energy in order to raise the energy ratio sufficiently to detect the tsunami arrival.

Regarding energy ratio, we revealed that the order of the energy ratio necessary for tsunami arrival detection by real-time analysis $O(10^{-1})$" was one order of magnitude less than that by *a posteriori* analysis $O(10^{0})$. This is because the tsunami energy is sufficiently accumulated in the *a posteriori* analysis since the time of detection was set to 60 min after manifestation, whereas the tsunami energy was barely accumulated in the real-time analysis since the tsunami arrival was detected a few minutes after manifestation. For the *a posteriori* analysis, the location where the corresponding energy ratio equals $O(10^{-1})$ was presented as far offshore beyond the continental shelf edge (cell 20). In these ranges, tsunami-induced velocity is rather small and larger BGN

prevents an increase of cross-correlation which delays detection. This is because it takes longer to raise the cross-correlation by accumulating the energy ratio.

Moreover, real-time detection probability was examined through comparison with a previous detection method using q-factor proposed by Lipa et al. (2012a, b, 2014). No misdetections were found and detection probability at the time of tsunami arrival was almost the same as that by q-factor with a threshold of ±500 in ranges from cell 2 to 15. Tsunami arrival was detected within 3–5 min (2–3 min delay compared with the time detected by q-factor) after the time of manifestation of tsunami-induced velocity. However, we believe that the delay would be resolved by using a shorter period to calculate the cross-correlation. It was found that the present method is superior in that it detects not only arrival of the tsunami wavefront but also subsequent tsunami wavetrains, whereas the detection method using q-factor is optimized to detect tsunami wavefront.

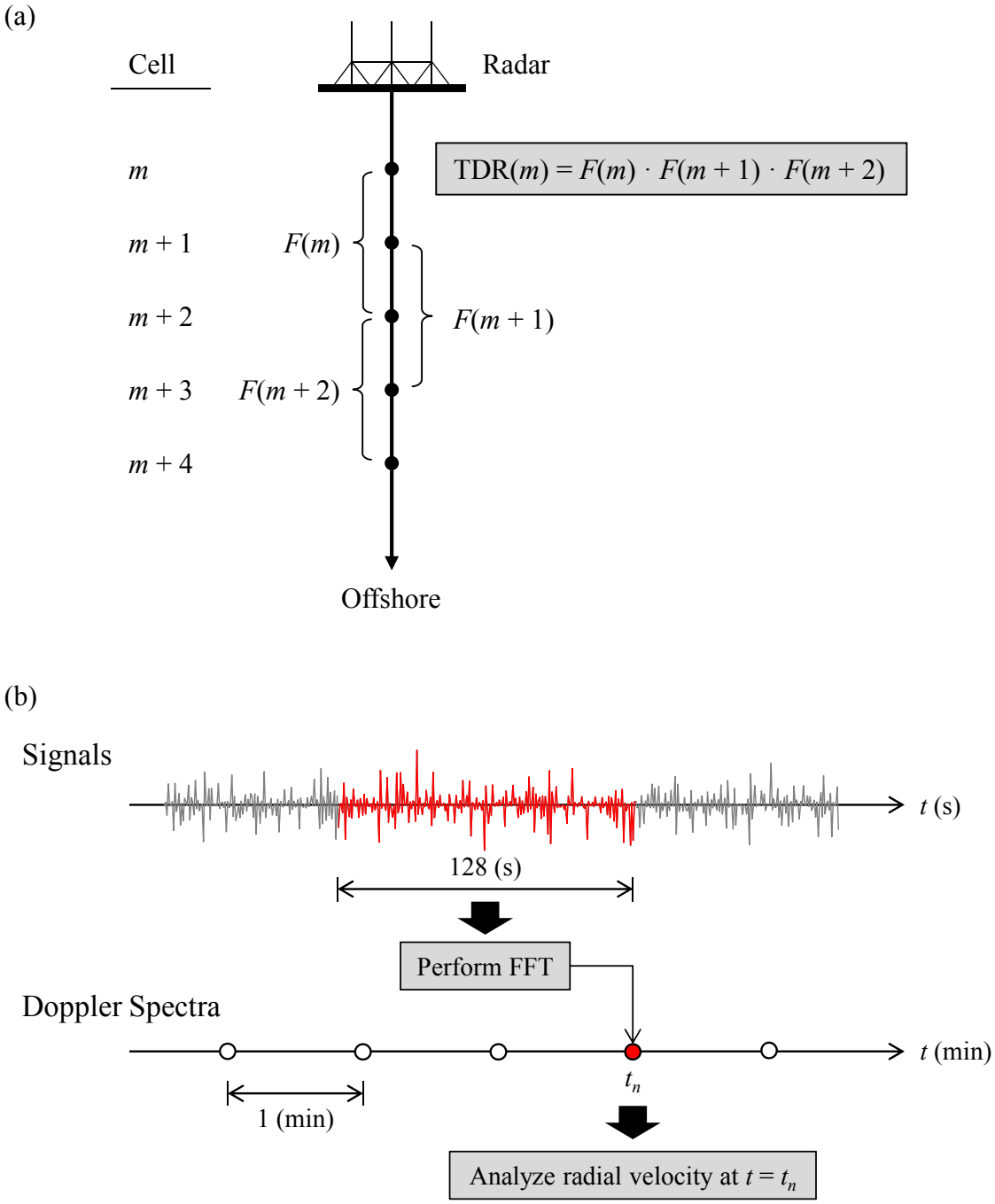

Fig. 3.1 Schematic illustration of a tsunami detection method in real-time analysis. **a** Definition of a tsunami detection factor and corresponding significance functions. **b** Relationship between location of signal periods (128 s) for calculating Doppler spectra and time of analyzed radial velocities. $v_{vt}(m, t_n)$, $v_{obs}(m, t_n)$, and $v_{sim}(m, t_n)$ were defined at $t = t_n$ (*red circle*)

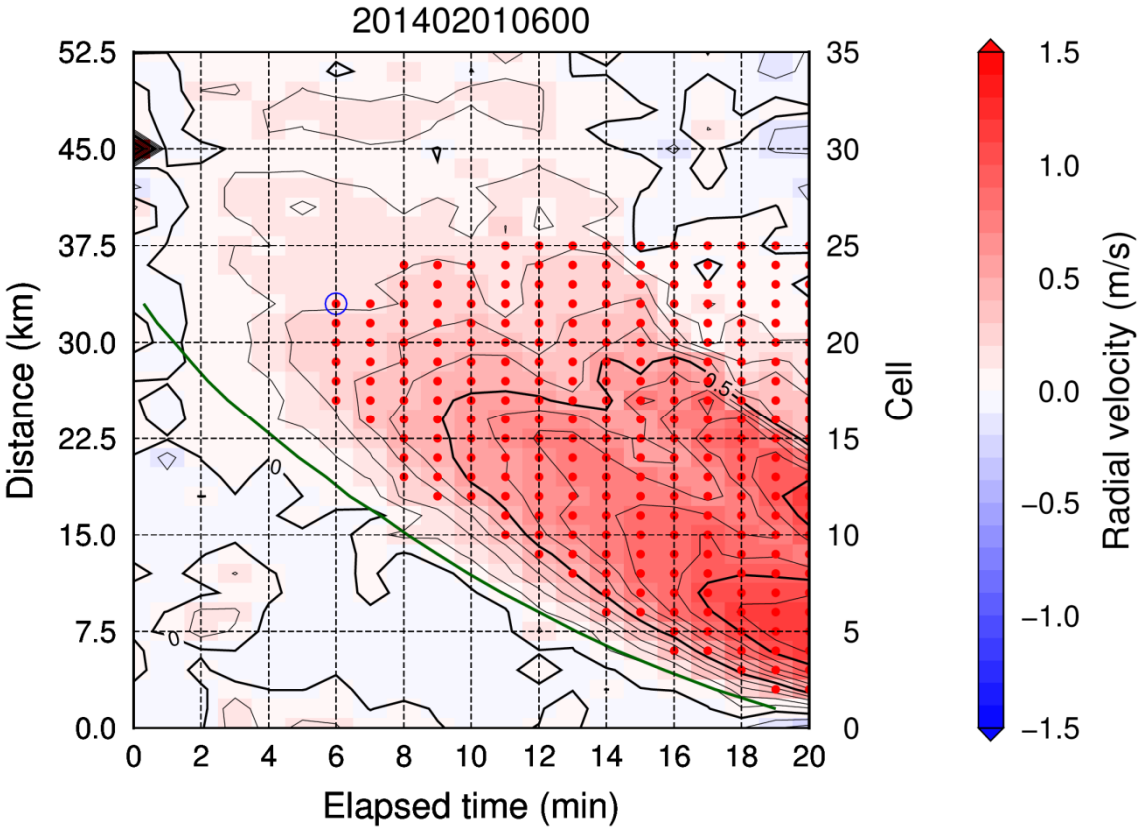

Fig. 3.2 Time–distance diagram of tsunami detection result in real time assuming the tsunami was excited at 06:00 on February 1, 2014. The *red circle* represents points where the tsunami was detected. The *green line* (theoretical tsunami wavefront) represents the theoretical curve obtained by back-calculating propagation from the speed of the linear long-wave starting from the time of tsunami arrival at the coast. The *background color contour* represents $v_{vt}(m, t_n)$

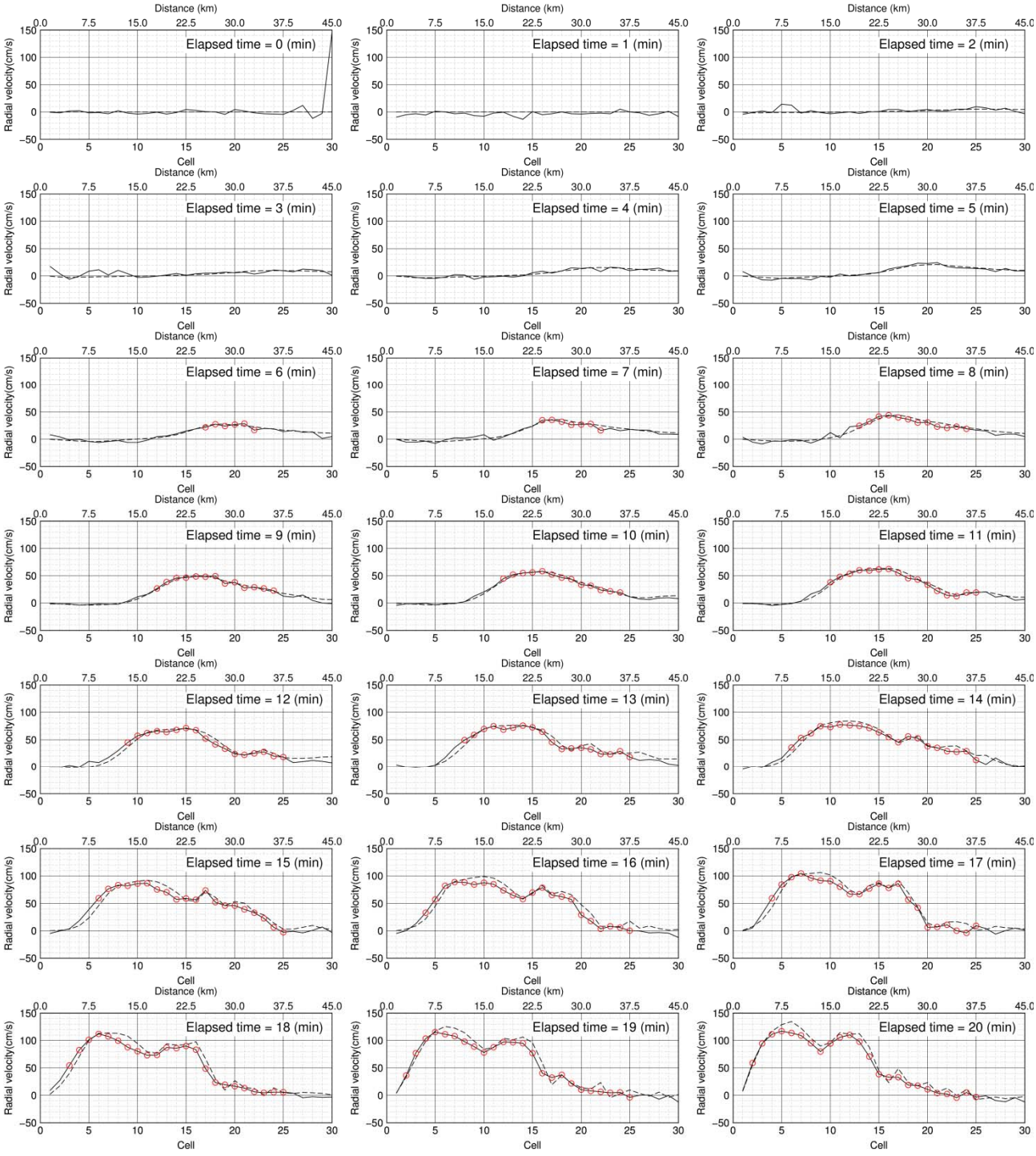

Fig. 3.3 Radial velocities of $v_{vt}(m, t_n)$ obtained by using a 60-min moving average and AR model (*solid*), and $v_{tsu}(m, t_n)$ (*dashed*) along the onshore-offshore direction after the occurrence of the tsunami in Fig. 3.2. The *red circle* represents the location where the tsunami was detected

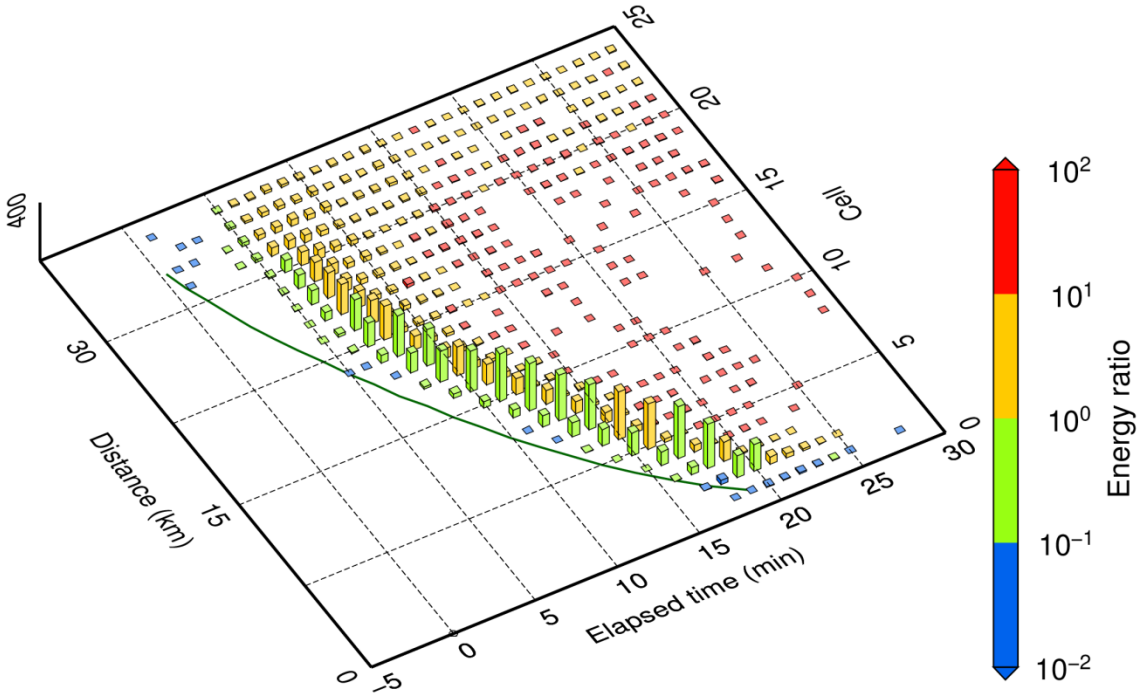

Fig. 3.4 Time–distance diagram of real-time detection result in February 2014. The *scale bar* is plotted at the time when the tsunami is detected for the first time in each range cell. The height of the *scale bar* represents the sum of the earliest detected events in each cell and the *color* represents the average energy ratio. The *green line* represents the theoretical tsunami wavefront

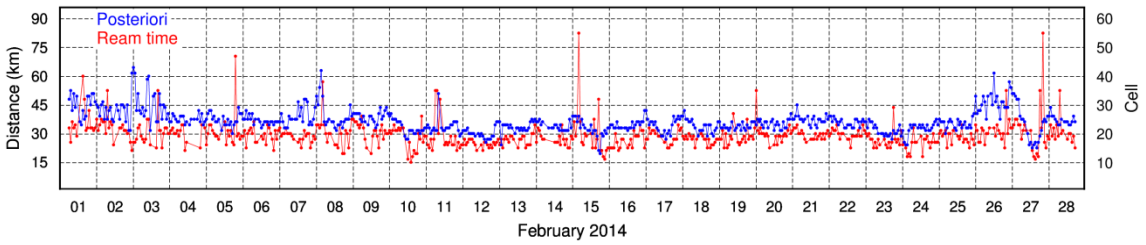

Fig. 3.5 Time–distance diagram of the maximum tsunami detection distance comparing real-time analysis (*red*) and *a posteriori* analysis (*blue*). The *blue line* is shifted by 4 cells (6 km) in the onshore direction

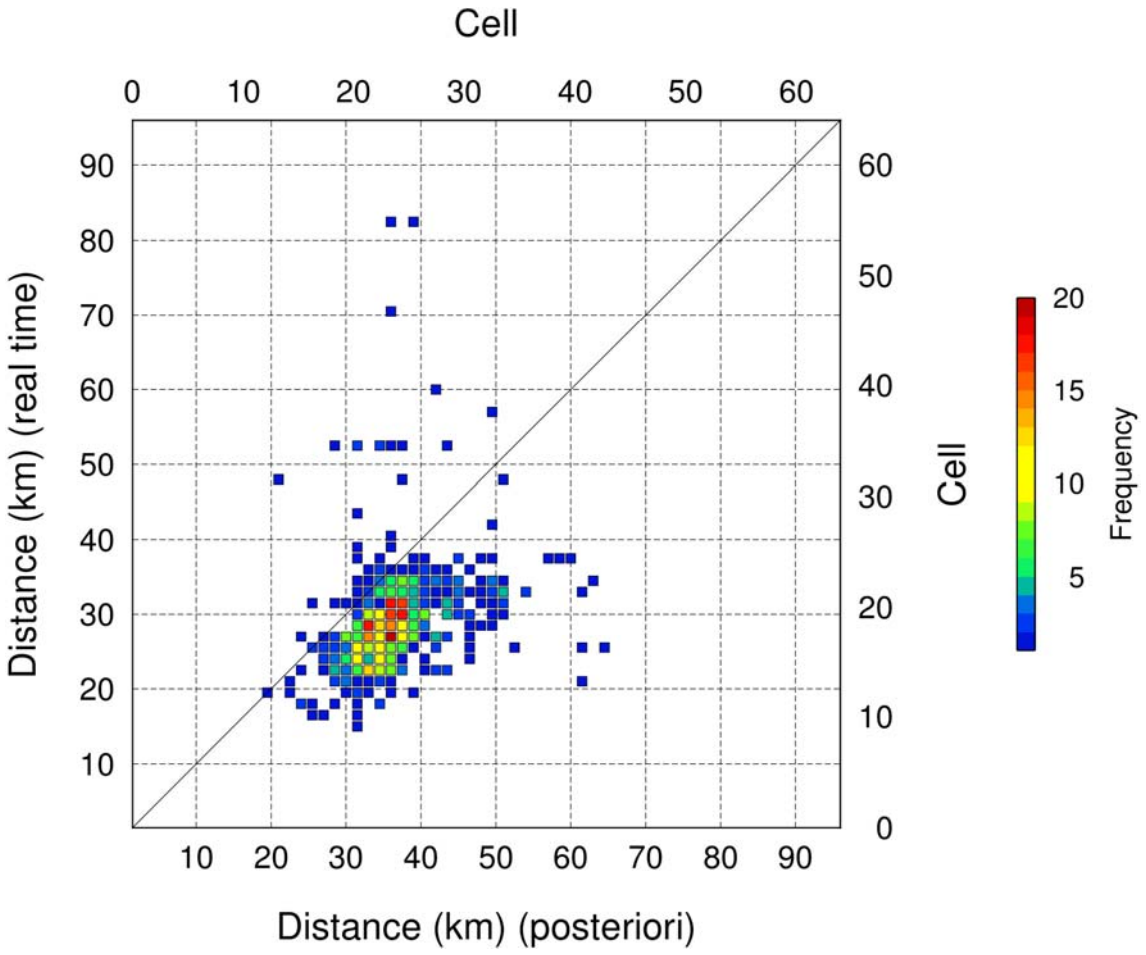

Fig. 3.6 Comparison of maximum detection range by real-time analysis and *a posteriori* analysis. The height of the color scale bar shows the frequency

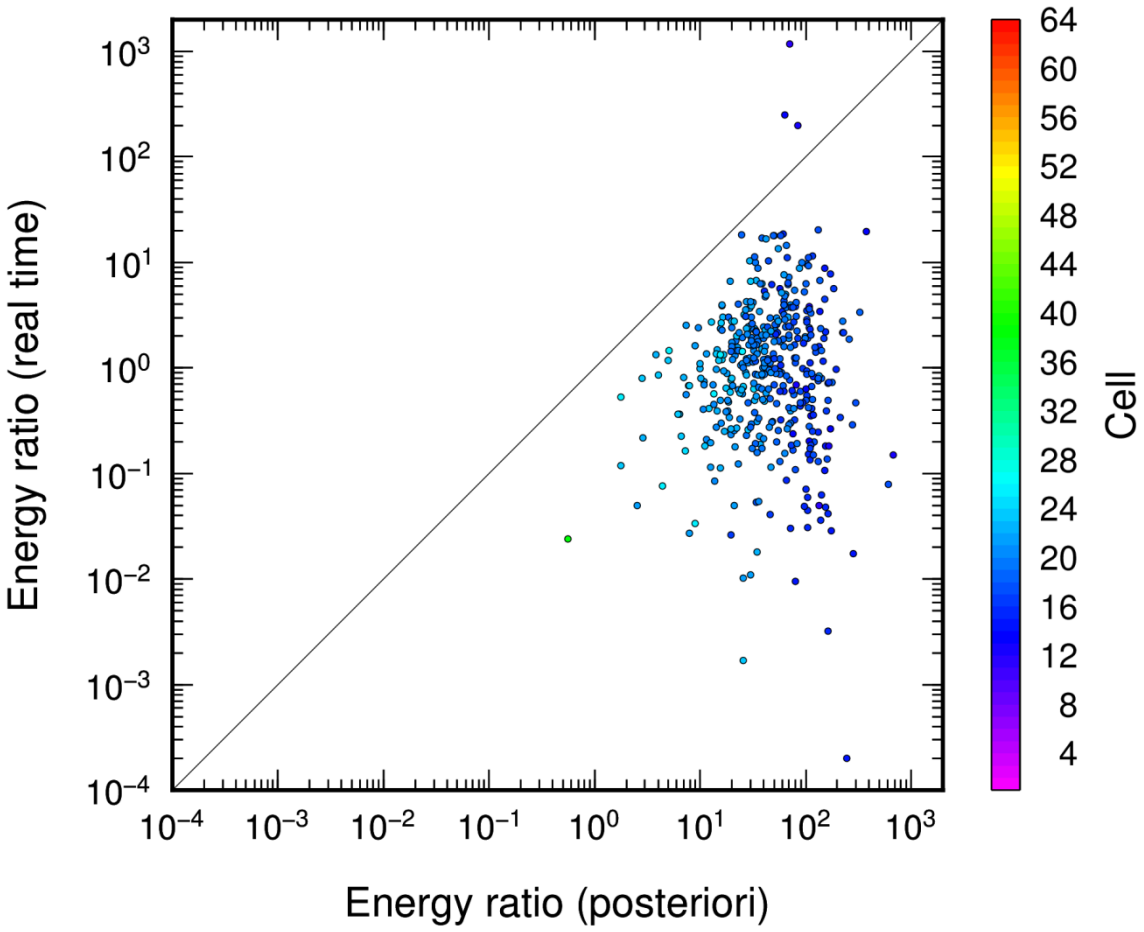

Fig. 3.7 Comparison of the energy ratio by real-time analysis and *a posteriori* analysis. The plot color corresponds to cell number. The energy ratio at the furthest location among the earliest detection times in each cell is plotted for real-time analysis and the energy ratio corresponding to the cell is plotted for *a posteriori* analysis

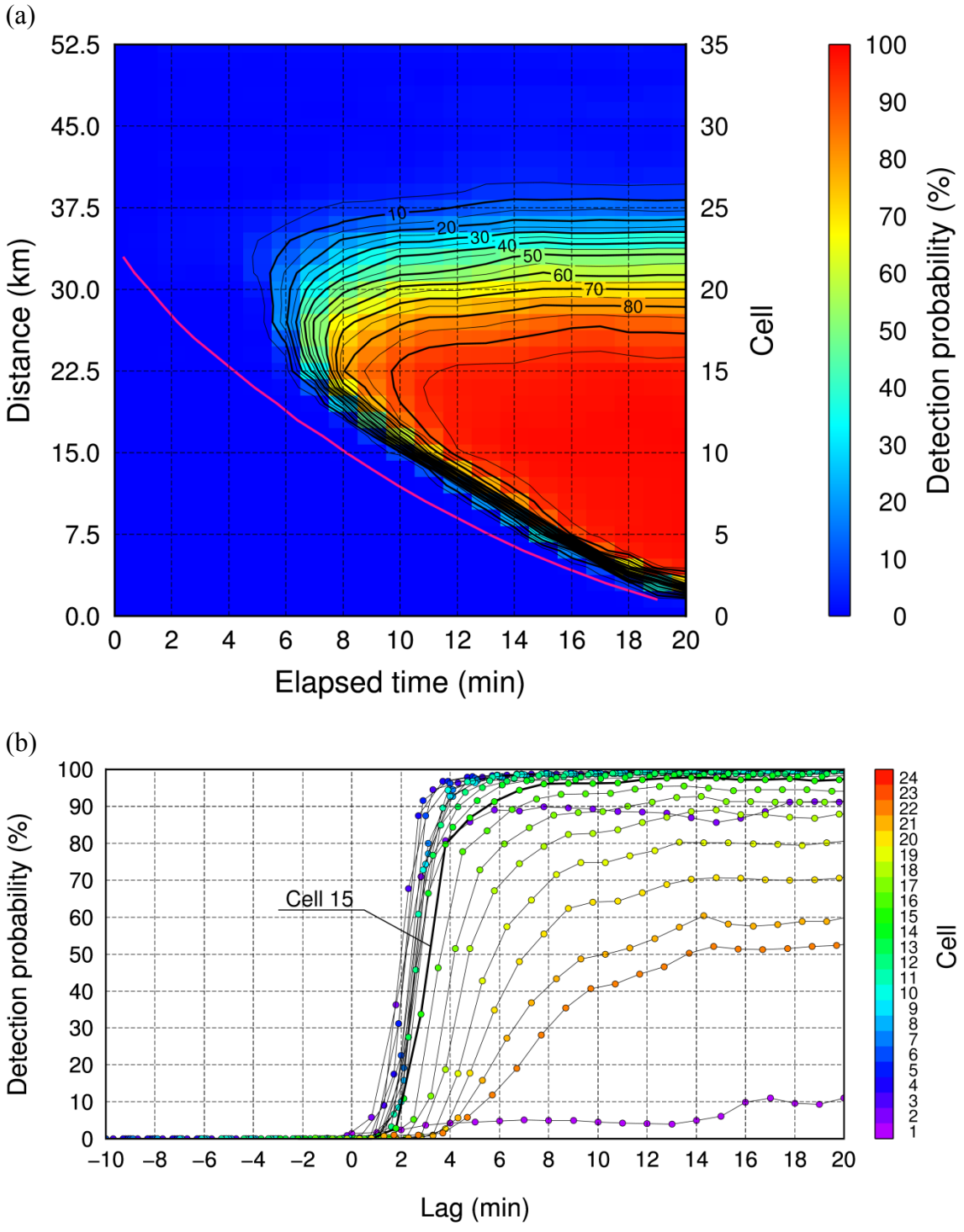

Fig. 3.8 a Contour plot of detection probability. The *pink line* represents the theoretical tsunami wavefront. **b** Dependence of the detection probability on time-lag, which means delay of tsunami detection, from the theoretical curve of tsunami propagation

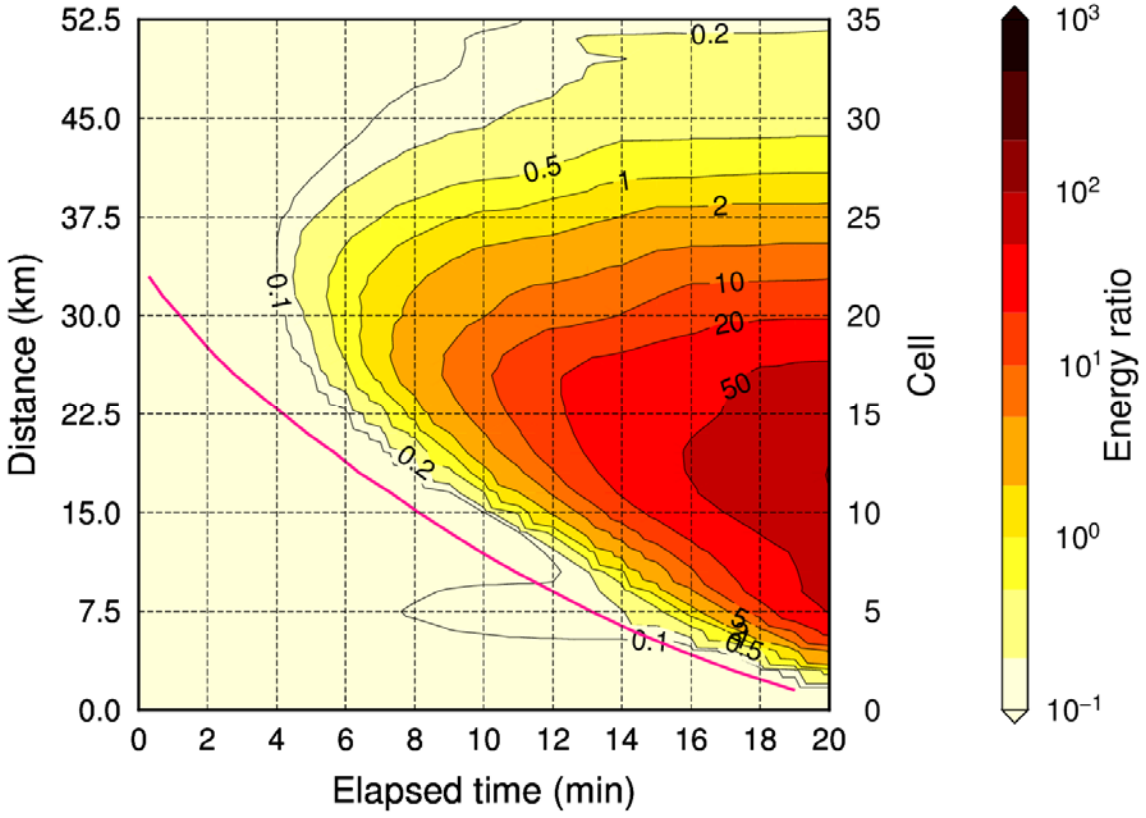

Fig. 3.9 Contour plot of average energy ratio. The *pink line* represents the theoretical tsunami wavefront

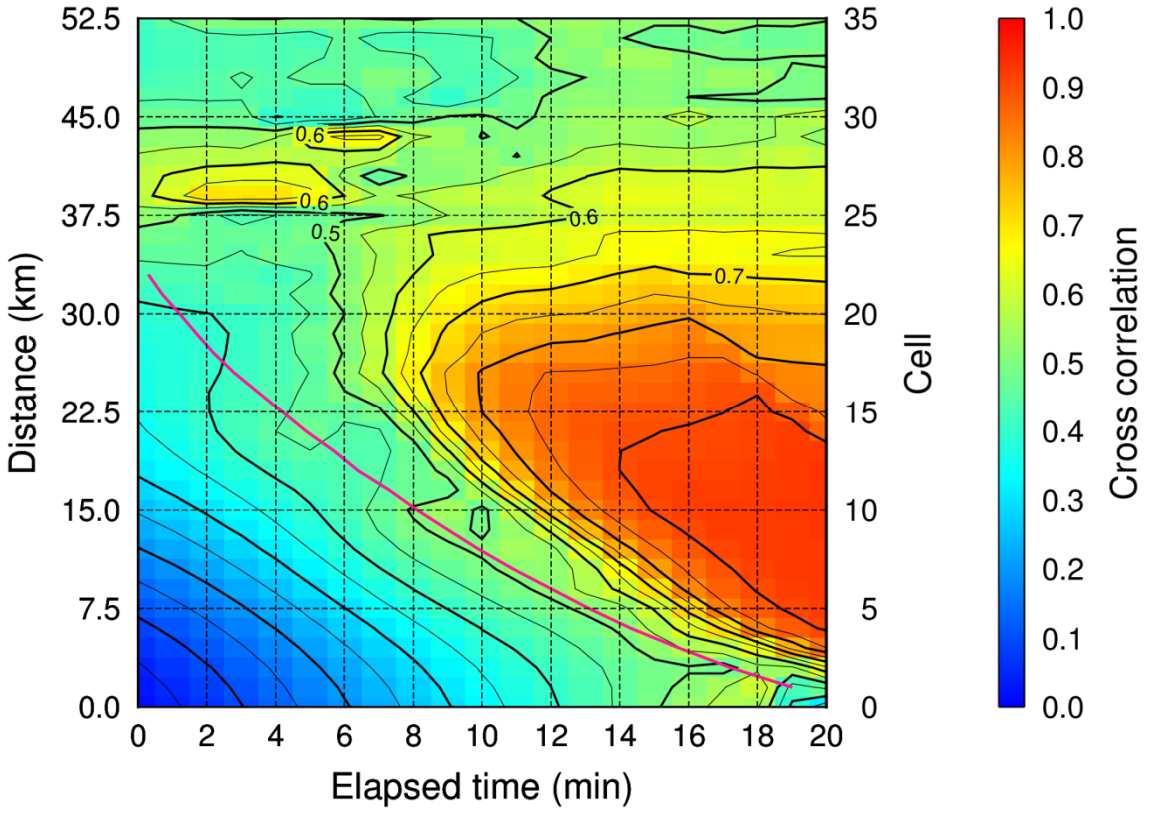

Fig. 3.10 Contour plot of average cross-correlation. The *pink line* represents the theoretical curve of tsunami propagation

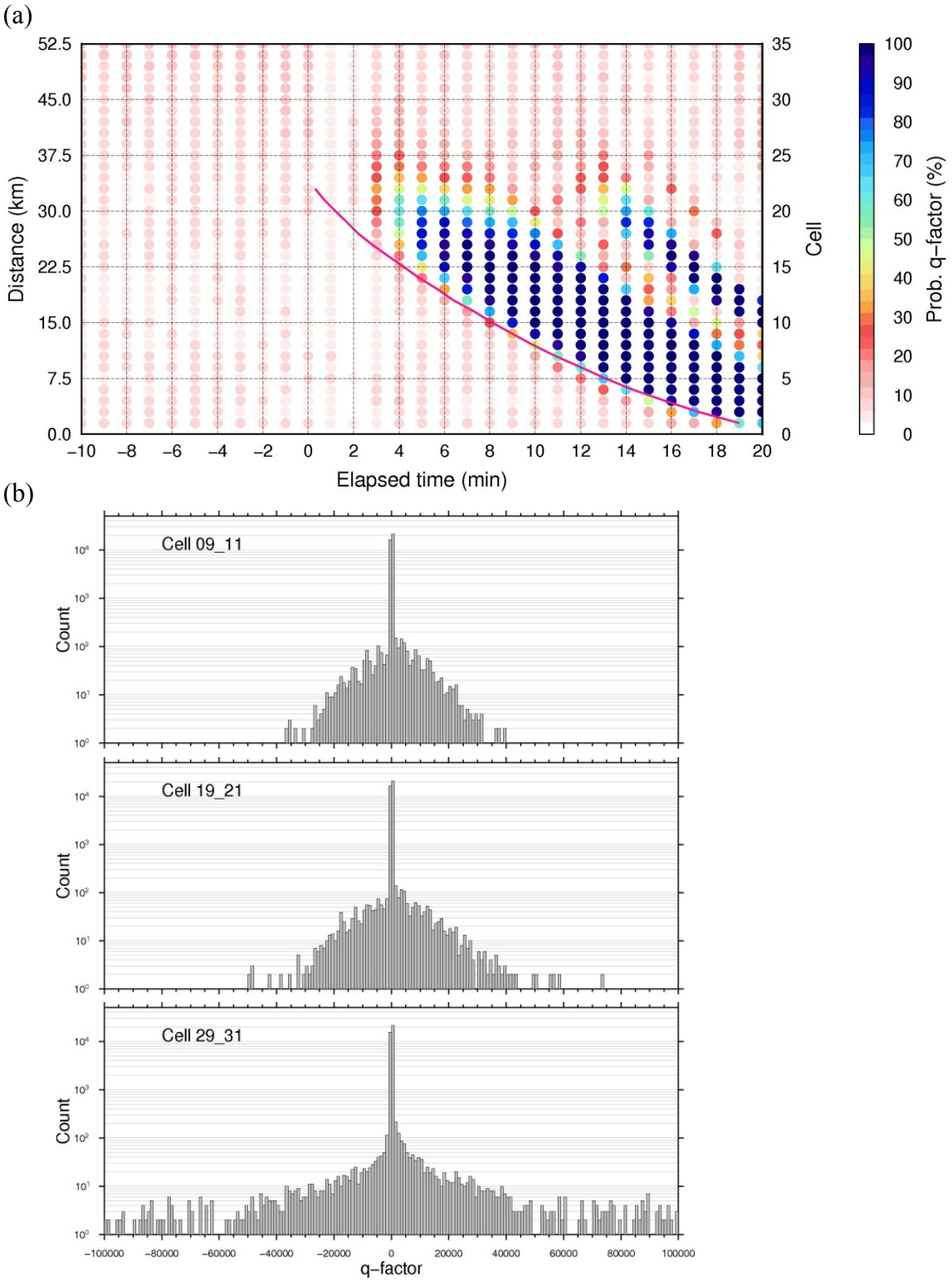

Fig. 3.11 Real-time detection probability of February 2014 using q-factor. The *pink line* represents the theoretical tsunami wavefront. **a** Time–distance diagram of detection probability when the threshold of q-factor was set to ±500. **b** Histogram of q-factor calculated from $v_{obs}(m, t_n)$ at cell 9 to 11, 19 to 21, and 29 to 30

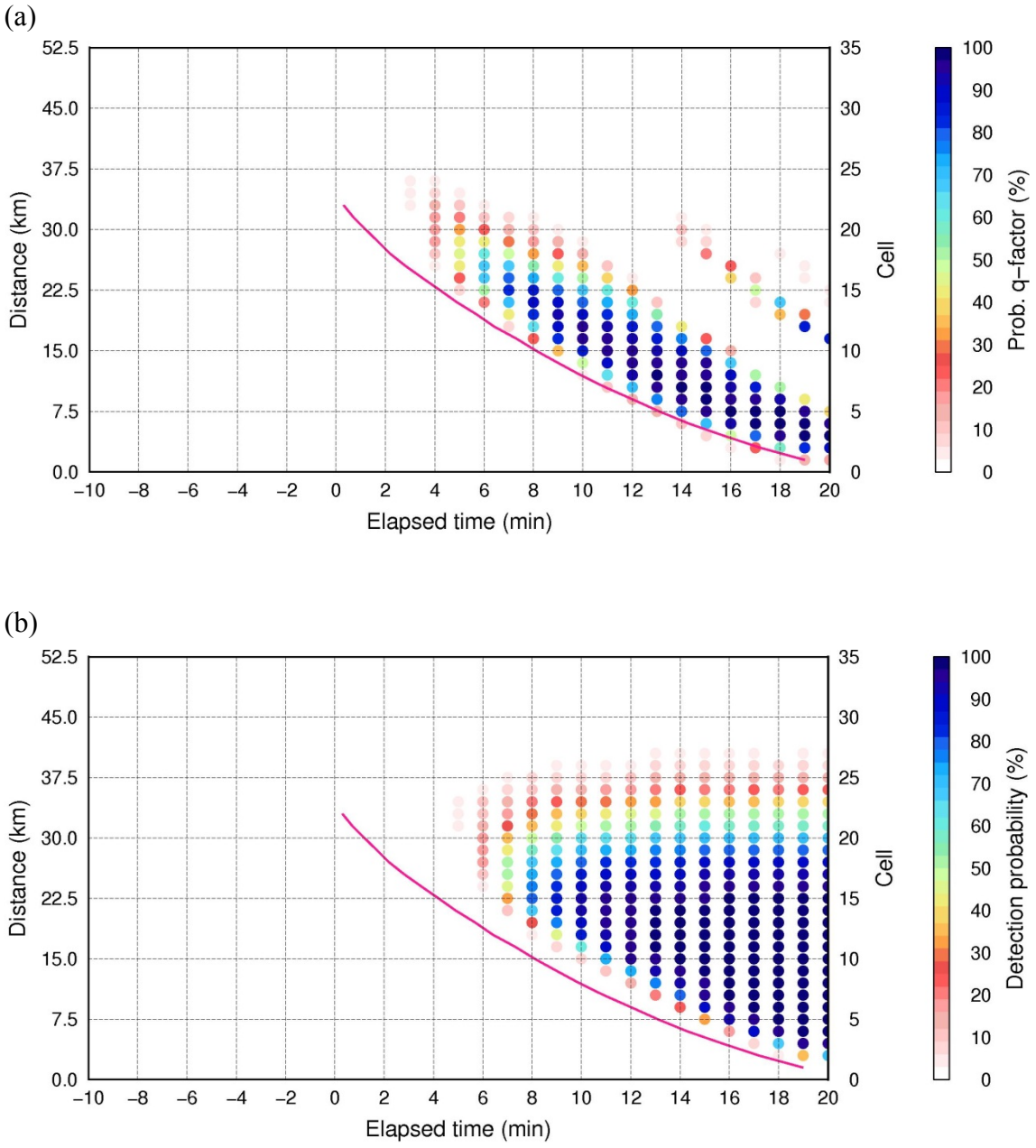

Fig. 3.12 Comparison of real-time detection probability of February 2014. The *pink line* represents the theoretical tsunami wavefront. **a** By q-factor when the threshold was set to ±100000 (200 times greater than that in Fig. 3.11a). b By present method using cross-correlation

Chapter 4

Conclusions

The tsunami generated by the March 11, 2011 Tohoku-Oki earthquake has changed awareness of tsunami disasters in Japan. At present, tsunami disaster mitigation is one of the most crucial problems Japan faces. Since HF radars have detected tsunami-induced velocity, they are expected to be useful for such mitigation. Thus, we investigated the tsunami detection performance of HF radar using the present detection method and discussed its effectiveness for mitigating tsunami disaster. We focused on statistical analysis to clarify the tsunami detection performance of HF radar because its detection probability presumably varies temporally due to the effects of ocean surface waves and SNR in addition to radar system specifications.

First, in Chapter 2, we statistically examined tsunami detection probability by using 1-month HF radar observation signals observed by NJRC radar installed on the Mihama coast in February 2014 and numerically simulated tsunami velocities induced by a M_w 9.0 Nankai Trough earthquake (Japan Cabinet Office's fault model case 3). In the examination, we performed virtual tsunami observation experiments to overcome

the difficulty of obtaining more tsunami observations through *a posteriori* analysis. From the experiment, we found that the possibility of tsunami detection primarily depends on the kinetic energy ratio between tsunami and shorter-period BGC velocities. In the onshore–offshore direction, the monthly average detection probability is over 90% when the energy ratio exceeds 5 (offshore distance: 9 km $\leq L \leq$ 36 km and water depth: 50 m $< h <$ 600 m) and is about 50% when the energy ratio is approximately 1 (L = 42 km, h = 1200 m). For a certain range cell on the radar beam, the energy ratio temporally varied in accordance with the variations of ocean surface wave height, ionospheric electron density and also with the shorter-period BGC physics. The results, namely that the tsunami detection distance strongly depends on the energy ratio between tsunami and shorter-period BGC velocities, and sea surface state as well as receiving noise, are the most important and general findings of the experiments. These demonstrate that virtual tsunami observation experiments for other seasons and/or for other coastal regions are required to comprehensively understand the tsunami detection performance of high-frequency radars.

Secondly, in Chapter 3, we examined the earliness of tsunami detection through real-time analysis. Evaluation of earliness of detection is of great importance for tsunami disaster mitigation in Japan. We found that the possibility of tsunami wavefront

detection primarily depends on the kinetic energy ratio even in real-time detection. However, the energy ratio required for tsunami wavefront detection is one order of magnitude less than that by *a posteriori* analysis. The maximum detection distance with 80% detection probability and 4-min time lag was 22.5 km (the corresponding energy ratio is of the order of 10^0). Tsunami arrival was detected approximately within 3–5 min after the time of manifestation of tsunami-induced velocity in ranges from 3 to 22.5 km with 80% probability. The established method is superior in terms of its ability to detect subsequent tsunami wavetrains in addition to tsunami wavefront, with no misdetection.

The method proposed in this study using cross-correlation is also outstanding in terms of its ability to detect tsunami in a quantitative manner and thus mitigate tsunami impact, such as to check the category of tsunami warning issued by the JMA, estimate tsunami height along the coast, and estimate the tsunami source based on the inversion method and thus specify areas at risk of devastating damage by numerical simulation, in addition to tsunami detection. HF radar can widely observe ocean surface currents. We examined the tsunami detection performance focusing on beam 04 in this study, but the present method can be easily applied to the whole observed area.

Acknowledgements

I would like to sincerely thank Ehime University for providing me with this precious opportunity to study as a doctoral student here. I am also indebted to my committee chair Professor Hirofumi Hinata of the Faculty of Engineering, Ehime University for his detailed guidance both in public and private, considerable encouragement and invaluable discussions that made my research possible and an unforgettable experience. I sincerely thank Professors Xinyu Guo, Ryo Moriwaki, and Shin'ichiro Mori for their valuable advice and comments on my thesis and presentation.

I am also very grateful to Professors Tomoyuki Takahashi of Kansai University, Satoshi Fujii of University of the Ryukyus, Takashi Tomita of Nagoya University, Akihiko Morimoto of Ehime University, Takayuki Suzuki of Yokohama National University, Dr. Tomoya Kataoka of the Tokyo University of Science, Dr. Shuji Seto of Kansai University, Dr. Tomohiro Takagawa of the Port and Airport Research Institute, Dr. Hiroaki Tsushima of Meteorological Research Institute, Dr. Keizo Hirano of Nagano Japan Radio Co., Ltd., Mr. Kenji Ueshima of the National Institute for Land and Infrastructure Management, Mr. Yoshihito Tanaka of Chubu Electric Power Co., Inc., Fumihiro Uehara of Chubu Electric Power Co., Inc., Ms. Megumi Okamoto of

Nippon Koei Co., Ltd., Mr. Yu Toguchi of University of the Ryukyus, and Mr. Kohei Ogata of Ehime University for their valuable comments and helpful discussions.

To Ms. Akari Otsuka, Dr. Yasuyuki Miyao, and the members of the Coastal Engineering Laboratory of Ehime University, I greatly enjoyed the opportunity to conduct the majority of my research with you. To Mr. Isamu Ogasawara and Mr. Hiroshi Nagamatsu of Kokusai Kogyo Co., Ltd., I am grateful for your support and encouragement.

Finally I sincerely thank my wife Kimiko and our son Jun'ichiro for their endless love, understanding, great support and encouragement throughout my research.

References

Barrick D (1971) Theory of HF and VHF propagation across the rough sea, 2, Application to HF and VHF propagation above the sea. Radio Sci 6(5):527–533

Barrick D (1979) A coastal radar system for tsunami warning. Remote Sens Environ 8:353–358

Cummins PR, Laura SLK, Satake K (2009) Tsunami science four years after the 2004 Indian Ocean tsunami: Part II Observation and data analysis. Pure Appl Geophys 166(1–7) Topical Issue

Dzvonkovskaya A (2012) Ocean surface current measurements using HF radar during the 2011 Japan tsunami hitting Chilean coast. In 2012 IEEE International Geoscience and Remote Sensing Symposium, pp 7605–7608. doi: 10.1109/IGARSS.2012.6351867

Dzvonkovskaya A, Figueroa D, Gurgel KW, Rohling H, Schlick T (2011) HF radar observation of a tsunami near Chile after the recent great earthquake in Japan. 12th International Radar Symposium, Leipzig, Germany, pp 125–130

Fuji R, Hinata H, Fujii S, Takahashi T (2013) Influences of time integration on the accuracy of inversion based on ocean radar. J Jpn Soc Civil Eng Ser B2 (Coastal Engineering) 69:436–440 (in Japanese with English abstract)

Fuji R, Hinata H, Fujii S, Nagamatsu H, Ogasawara I, Ito H, Kataoka T, Takahashi T (2015) Tsunami detection based on virtual tsunami observation experiment by using oceanographic radar. J Jpn Soc Civil Eng Ser B2 (Coastal Engineering) 71:337–342 (in Japanese with English abstract)

Fuji R, Hinata H (2017) Temporal variability of tsunami arrival detection distance revealed by virtual tsunami observation experiments using numerical simulation and 1-month HF radar observation. J Oceanogr. doi: 10.1007/s10872-017-0428-y (in press)

Goto C, Ogawa Y, Shuto N, Imamura F (1997) IUGG/IOC time project: Numerical method of tsunami simulation with the leap-frog scheme. Intergov Oceanogr Comm Man Guides 35

Grilli ST, Grosdidier S, Guerin CA (2015) Tsunami detection by high-frequency radar beyond the continental shelf. Pure Appl Geophys 1–40. doi: 10.1007/s00024-015-1193-8

Grilli ST, Shelby M, Grilli AR, Guérin CA, Grosdidier S, Lado IT (2016) Algorithms for tsunami detection by high frequency radar: development and case studies for tsunami impact in British Columbia, Canada. In: Proceedings of the 26th Offshore and Polar Engineering Conference (ISOPE16, Rodos, Greece, June 2016), International Society of Offshore and Polar Engineers, pp 807–814. http://personal.egr.uri.edu/grilli/Grilli_etal_2016_HFradar.pdf. Accessed 1 Nov 2016

Gurgel KW, Dzvonkovskaya A, Pohlmann T, Schlick T, Gill EW (2011) Simulation and detection of tsunami signatures in ocean surface currents measured by HF radar. Ocean Dyn 61(10):1495–1507. doi: 10.1007/s10236-011-0420-9

Hinata H, Fujii S, Furukawa K, Kataoka T, Miyata M, Kobayashi T, Mizutani M, Kokai T, Kanatsu N (2011) Propagating tsunami wave and subsequent resonant response signals detected by HF radar in the Kii Channel, Japan. Estuary Coast Shelf S 95(1):268–273. doi: 10.1016/j.ecss.2011.08.009

Hinata H, Fuji R, Fujii S, Fujita Y, Hanado H, Kataoka T, Mizutani M, Takahashi T (2012) HF radar observation of velocity fields induced by tsunami waves in the Kii Channel, Japan. J Jpn Soc Civil Eng Ser B2 (Coastal Engineering) 68:196–200 (in Japanese with English abstract)

Imai K, Satake K, Furumura T (2010) Amplification of tsunami heights by delayed rupture of great earthquakes along the Nankai Trough. Earth Planets Space 62(4):427–432. doi: 10.5047/eps.2009.12.005

Ishii M (2009) Studies of ionospheric variations for radio propagation. J Natl Inst Inf Commun Technol 56(1–4):223–229

Lipa B, Barrick D, Bourg J, Nyden B (2006) HF radar detection of tsunamis. J Oceanogr 62:705–716. doi: 10.1007/s10872-006-0088-9

Lipa B, Barrick D, Saitoh S, Ishikawa Y, Awaji T, Largier J, Garfield N (2011) Japan tsunami current flows observed by HF radars on two continents. Remote Sens 3(8):1663–1679. doi: 10.3390/rs3081663

Lipa B, Isaacson J, Nyden B, Barrick D (2012a) Tsunami arrival detection with high frequency (HF) radar. Remote Sens 4(5):1448–1461. doi:10.3390/rs4051448

Lipa B, Barrick D, Diposaptono S, Isaacson J, Jena BK, Nyden B, Rajesh K, Kumar TS (2012b) High frequency (HF) radar detection of the weak 2012 Indonesian tsunamis. Remote Sens 4(10):2944–2956. doi:10.3390/rs4102944

Lipa B, Parikh H, Barrick D, Roarty H, Glenn S (2014) High-frequency radar observations of the June 2013 US East Coast meteotsunami. Nat Hazards 74(1):109–122. doi: 10.1007/s11069-013-0992-4

Okada Y (1992) Internal deformation due to shear and tensile faults in a half-space. Bull Seismol Soc Am 82(2):1018–1040

Ozaki T (2011) Outline of the 2011 off the Pacific coast of Tohoku Earthquake (M_w 9.0)—Tsunami warnings/advisories and observations—. Earth Planets Space 63:827–830. doi: 10.5047/eps.2011.06.029

Rohling H (1983) Radar CFAR thresholding in clutter and multiple target situations. IEEE Trans Aerosp Electron Syst AES 19:608–621

Satake K (1987) Inversion of tsunami waveforms for the estimation of a fault heterogeneity: Method and numerical experiments. Jour Phys Earth 35:241–254

Seto S, Takahashi T (2015) Examination on the observation site of oceanographic radar for tsunami source and propagation in the Nankai Trough. J Jpn Soc Civil Eng Ser B2 (Coastal Engineering) 71:343–348 (in Japanese with English abstract)

Sugawara D, Goto K (2012) Numerical modeling of the 2011 Tohoku-oki tsunami in the offshore and onshore of Sendai Plain, Japan. Sediment Geol 282:110–123. doi:10.1016/j.sedgeo.2012.08.002

Takahashi T, Takahashi T, Shuto N, Imamura F, Ortiz M (1995) Source models for the 1993 Hokkaido Nansei-Oki earthquake tsunami. Pure Appl Geophys 144:747–767. doi: 10.1007/BF00874393

Takahashi T, Konuma T (2011) Verification of disaster management information on the 2004 Indonesian Ocean tsunami using virtual tsunami warning system. Journal of Disaster Research 6(2):212–218. doi: 10.20965/jdr.2011.p0212

Tsushima H, Hino R, Fujimoto H, Tanioka Y, Imamura F (2009) Near-field tsunami forecasting from cabled ocean bottom pressure data. J Geophys Res 114, B06309. doi: 10.1029/2008JB005988

Tsushima H, Hirata K, Hayashi Y, Tanioka Y, Kimura K, Sakai S, Shinohara M, Kanazawa T, Hino R, Maeda K (2011) Near-field tsunami forecasting using offshore tsunami data from the 2011 off the Pacific coast of Tohoku Earthquake. Earth Planets Space 63:821–826. doi: 10.5047/eps.2011.06.052

Tsushima H, Hino R, Tanioka Y, Imamura F, Fujimoto H (2012) Tsunami waveform inversion incorporating permanent seafloor deformation and its application to tsunami forecasting. J Geophys Res 117, B03311, doi: 10.1029/2011JB008877